



# Impacts of Bar-driven Shear and Shocks on Star Formation

Taehyun Kim<sup>1</sup>, Dimitri A. Gadotti<sup>2</sup>, Miguel Querejeta<sup>3</sup>, Isabel Pérez<sup>4,5</sup>, Almudena Zurita<sup>4,5</sup>, Justus Neumann<sup>6</sup>, Glenn van de Ven<sup>7</sup>, Jairo Méndez-Abreu<sup>8,9</sup>, Adriana de Lorenzo-Cáceres<sup>8,9</sup>, Patricia Sánchez-Blázquez<sup>10,11</sup>, Francesca Fragkoudi<sup>12</sup>, Lucimara P. Martins<sup>13</sup>, Luiz A. Silva-Lima<sup>13</sup>, Woong-Tae Kim<sup>14,15</sup>, and Myeong-Gu Park<sup>1,16</sup>

<sup>1</sup> Department of Astronomy and Atmospheric Sciences, Kyungpook National University, Daegu 702-701, Republic of Korea; [tkim.astro@gmail.com](mailto:tkim.astro@gmail.com), [mgp@knu.ac.kr](mailto:mgp@knu.ac.kr)

<sup>2</sup> Centre for Extragalactic Astronomy, Department of Physics, Durham University, South Road, Durham DH1 3LE, UK

<sup>3</sup> Observatorio Astronómico Nacional, C/Alfonso XII 3, Madrid 28014, Spain

<sup>4</sup> Departamento de Física Teórica y del Cosmos, Campus de Fuentenueva, Universidad de Granada, 18071 Granada, Spain

<sup>5</sup> Instituto Carlos I de Física Teórica y Computacional, Facultad de Ciencias, 18071 Granada, Spain

<sup>6</sup> Max Planck Institute for Astronomy, Königstuhl 17, 69117, Germany

<sup>7</sup> Department of Astrophysics, University of Vienna, Türkenschanzstraße 17, 1180 Vienna, Austria

<sup>8</sup> Instituto de Astrofísica de Canarias, Calle Vía Láctea s/n, 38205 La Laguna, Tenerife, Spain

<sup>9</sup> Departamento de Astrofísica, Universidad de La Laguna, 38200 La Laguna, Tenerife, Spain

<sup>10</sup> Departamento de Física de la Tierra y Astrofísica, Universidad Complutense de Madrid, E-28040 Madrid, Spain

<sup>11</sup> Instituto de Física de Partículas y del Cosmos (IPARCOS), Universidad Complutense de Madrid, E-28040, Spain

<sup>12</sup> Institute for Computational Cosmology, Department of Physics, Durham University, South Road, Durham DH1 3LE, UK

<sup>13</sup> Universidade Cidade de São Paulo/Universidade Cruzeiro do Sul, Rua Galvão Bueno 868, São Paulo-SP, 01506-000, Brazil

<sup>14</sup> Department of Physics & Astronomy, Seoul National University, Seoul 08826, Republic of Korea

<sup>15</sup> SNU Astronomy Research Center, Seoul National University, Seoul 08826, Republic of Korea

Received 2023 December 26; revised 2024 April 3; accepted 2024 April 19; published 2024 June 14

## Abstract

Bars drive gas inflow. As the gas flows inward, shocks and shear occur along the bar dust lanes. Such shocks and shear can affect the star formation (SF) and change the gas properties. For four barred galaxies, we present  $H\alpha$  velocity gradient maps that highlight bar-driven shocks and shear using data from the PHANGS-MUSE and PHANGS-ALMA surveys, which allow us to study bar kinematics in unprecedented detail. Velocity gradients are enhanced along the bar dust lanes, where shocks and shear are shown to occur in numerical simulations. Velocity gradient maps also efficiently pick up H II regions that are expanding or moving relative to the surroundings. We put pseudo-slits on the regions where velocity gradients are enhanced and find that  $H\alpha$  and CO velocities jump up to  $\sim 170 \text{ km s}^{-1}$ , even after removing the effects of circular motions due to the galaxy rotation. Enhanced velocity gradients either coincide with the peak of CO intensity along the bar dust lanes or are slightly offset from CO intensity peaks, depending on the objects. Using the Baldwin–Philips–Terlevich BPT diagnostic, we identify the source of ionization on each spaxel and find that SF is inhibited in the high-velocity gradient regions of the bar, and the majority of those regions are classified as a low-ionization nuclear emission-line region (LINER) or composite. This implies that SF is inhibited where bar-driven shear and shocks are strong. Our results are consistent with the results from the numerical simulations that show SF is inhibited in the bar where the shear force is strong.

*Unified Astronomy Thesaurus concepts:* Barred spiral galaxies (136); Spiral galaxies (1560); Galaxy structure (622); Star formation (1569); Galaxy kinematics (602)

## 1. Introduction

Numerical simulations and observations find that once a galactic disk is massive enough and dynamically cold, it is often easy to form bars (e.g., Hohl 1971; Ostriker & Peebles 1973; Combes & Sanders 1981; Athanassoula & Misiriotis 2002; Kraljic et al. 2012; Sheth et al. 2012; Seo et al. 2019; Fragkoudi et al. 2020). Bars are frequently found in nearby galaxies, and the fraction of barred galaxies exceeds 65%, including weak bars (e.g., de Vaucouleurs 1963; Eskridge et al. 2000; Menéndez-Delmestre et al. 2007; Barazza et al. 2008; Aguerri et al. 2009; Masters et al. 2011; Buta et al. 2015; Díaz-García et al. 2016; Lee et al. 2019). Bars are nonaxisymmetric structures inducing tangential forces and gravitational torques on the gas. As the gas around the bar within the corotation

radius loses angular momentum, it flows inward. Piled-up gas in the central region ignites active star formation (SF; Hawarden et al. 1986; Knapen et al. 1995; Sheth et al. 2005) to form nuclear disks that lead to the formation of inner bars in the nuclear disks and nuclear rings in some galaxies (e.g., Sormani et al. 2018a; de Lorenzo-Cáceres et al. 2019; Seo et al. 2019; Gadotti et al. 2020; Bittner et al. 2021; de Sá-Freitas et al. 2023a, 2023b). The gas transported to the central 100 pc may feed active galactic nuclei (AGN; e.g., Storchi-Bergmann & Schnorr-Müller 2019; Silva-Lima et al. 2022; Garland et al. 2023; Kolcu et al. 2023), although the connection between bars and AGN is still controversial (e.g., Ho et al. 1997; Knapen et al. 2000; Laine et al. 2002; Cisternas et al. 2013; Cheung et al. 2015; Neumann et al. 2019; Zee et al. 2023). Moreover, bars also enrich the diversity of the outer part of galaxies. Bars are frequently accompanied by an inner and outer ring and also induce spiral arms (e.g., Salo et al. 2010; Comerón et al. 2014; Buta et al. 2015).

In addition to structure and morphology, there are significant differences in the observed kinematics between barred and unbarred disk galaxies. Unbarred disk galaxies show

<sup>16</sup> Corresponding author.

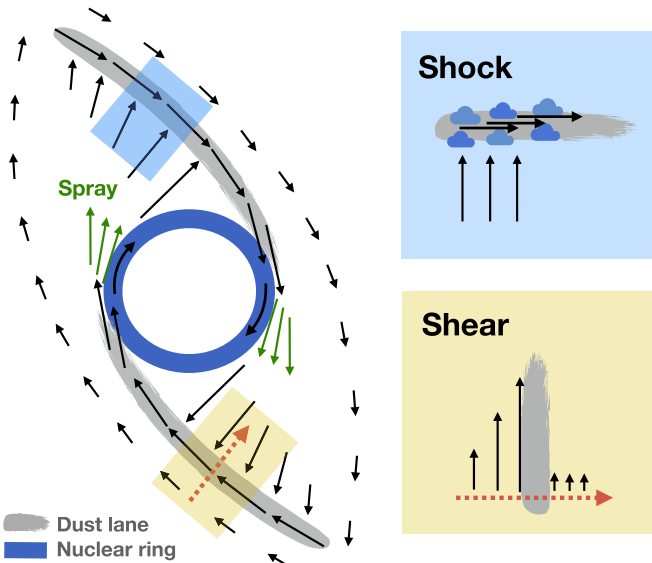


**Figure 1.** Schematic diagram of gas dynamics in the bar region. The magnitude and direction of gas particles are denoted by black arrows. Gas particles stream along the bar dust lane (thick gray lines). Some of them flow into the nuclear ring (blue circle), while others overshoot and spray into the other dust lane. On the right, the bar-driven shocks and shear are described. Gas particles are compressed in the dust lane. As gas enters the dust lane, the gas velocity is changed abruptly in direction and magnitude and thus experiences shocks. In the lower right panel, only the gas velocity vectors that are parallel to the dust lane are plotted. Shear occurs when there is a velocity gradient across the flow, perpendicular to the dust lane (orange dotted arrow) in this case.

isovelocity maps that can be well explained by circular motions (e.g., Bosma 1981), while barred galaxies exhibit characteristic “S-shaped” bends along the bar in isovelocity diagrams (e.g., Peterson & Huntley 1980; Fathi et al. 2005; López-Cobá et al. 2022). Due to the nonaxisymmetric structure, both gas and stellar kinematics are affected. Gas in the bar region experiences noncircular, streaming motions, which are estimated to be  $\sim 40\text{--}100\text{ km s}^{-1}$  (Rozas et al. 2000; Zurita et al. 2004). Stars in the bar region are thought to follow  $x1$  orbits which are elongated along the major axis of the bar, and also  $x2$  orbits that are rounder, and elongated perpendicular to the bar (e.g., Contopoulos & Papayannopoulos 1980).

In Figure 1, we present a schematic diagram that describes the direction and magnitude of gas velocities within the bar region. Gas flows inward along the bar dust lanes, which are found at locations of hydrodynamic shocks based on simulations (e.g., Roberts et al. 1979; Athanassoula 1992; Sormani et al. 2015; Fragkoudi et al. 2017). If there is a nuclear ring, a part of the gas ( $\sim 20\%$ – $30\%$ , Regan et al. 1997; Hatchfield et al. 2021) enters the nuclear ring, while the remaining gas overshoots and sprays toward the other bar dust lane (e.g., Sormani et al. 2019). In the right panel of Figure 1, shocks and shear are described in the blue and orange boxes, respectively. When the gas particles are sprayed and encounter the other bar dust lane, the gas particles are suddenly decelerated, and both the direction and the magnitude of the gas velocities are abruptly changed (see, e.g., Figures 7 and 8 of Kim et al. 2012a). This mechanism makes dissipative gas particles experience shocks. As gas particles flow into the dust lane, they also experience large velocity shear. The shear occurs when there are velocity gradients across the flow, here perpendicular to the dust lane. To highlight shear motions, only the gas velocity vectors that are parallel to the dust lane

are drawn on the right bottom panel of Figure 1. There are velocity gradients along the orange dotted arrow, which lead to velocity shear. More details from simulated barred galaxies can be found in Figure 2 of Athanassoula (1992), Figure 10 of Downes et al. (1996), Figure 9 of Regan et al. (1999), Figure 7(a) of Kim et al. (2012a), and Figures 8 and 9 of Sormani et al. (2018b).

Using hydrodynamic simulations, Kim et al. (2012a) investigate the formation and properties of various substructures of barred galaxies. They find strong velocity shear across the bar dust lane amounting to  $\sim 1\text{--}3\text{ km s}^{-1}\text{ pc}^{-1}$ , which is  $\sim 10$  times larger than the shear from the Galactic rotation in the solar neighborhood.

Gas flows into the central regions of the galaxy along the bar dust lanes (e.g., Athanassoula 1992; Englmaier & Gerhard 1997; Kim et al. 2012a; Fragkoudi et al. 2016; Sormani et al. 2023), and as the bar-driven shocks and shear occur right at the dust lane, it is one of the most interesting sites to test the influence of shocks and shear on SF. In this study, we aim to examine whether SF is promoted or suppressed along the bar where strong shear and shocks are expected.

The loci of SF and star formation rate (SFR) vary among barred galaxies (e.g., Verley et al. 2007; Neumann et al. 2019; Díaz-García et al. 2020; Fraser-McKelvie et al. 2020; George et al. 2020). Detailed studies on individual galaxies found that SF in the bar region is low (e.g., Tubbs 1982), although the gas column densities in the bar dust lanes are high (Sheth et al. 2000). Star formation efficiency (SFE) is found to be low in the bar region compared to other regions in the disk (Momose et al. 2010; Hirota et al. 2014; Muraoka et al. 2016; Yajima et al. 2019; Maeda et al. 2020, 2023; Pessa et al. 2022).

However, studies on larger samples give different results and find that SFE in the bar region is not systematically lower compared to that in the other regions (e.g., Muraoka et al. 2019; Díaz-García et al. 2021; Querejeta et al. 2021). Díaz-García et al. (2021) report that SFE in strong bars is not systematically inhibited, and the SFEs are roughly constant along bars. Using data from the PHANGS-ALMA survey, Querejeta et al. (2021) define five environments within galaxies (center, bar, spiral arm, interarm region, and disk without strong spirals) and find that the SFR surface density in bars is comparable to that in spiral arms and higher than those in disks and interarm regions.

Spatial resolution may play a role in resolving the detailed structures in the bar region (e.g., nuclear rings). Large integral field spectroscopy surveys (e.g., CALIFA, Sánchez et al. 2012, MaNGA, Bundy et al. 2015) typically have an average spatial resolution of  $\sim 1\text{--}2\text{ kpc}$ , and therefore, often cannot resolve nuclear rings, nuclear disks, or other smaller structures or star-forming sites. On the other hand, recent surveys such as TIMER (Gadotti et al. 2019), PHANGS-ALMA (Leroy et al. 2021a, 2021b) and PHANGS-MUSE (Emsellem et al. 2022) provide more resolved data sets (with spatial resolution  $\lesssim 100\text{ pc}$ ). However, different results on SFR and SFE do not seem to be particularly affected by different resolutions. The main difference may arise from the definition of the bar ends. Because the SF in bar ends is often high and efficient for some galaxies (e.g., Martin & Friedli 1997; Hirota et al. 2014; Renaud et al. 2015; Beuther et al. 2017; Yajima et al. 2019), including the bar ends (e.g., Querejeta et al. 2021) or excluding the bar ends (e.g., Maeda et al. 2023) in analyzing SFE in bar regions would yield different results. The differences may also

**Table 1**  
Basic Properties of Sample Galaxies

Galaxy	Type	Log $M_{\text{star}}$ ( $M_{\odot}$ )	Distance (Mpc)	Log(SFR) ( $M_{\odot} \text{ yr}^{-1}$ )	$V_{\text{sys}}$ ( $\text{km s}^{-1}$ )	PA <sub>disk</sub> (deg)	PA <sub>bar</sub> (deg)	Incl. (deg)	Scale (pc arcsec <sup>-1</sup> )	COPT PSF (arcsec)
(1)	(2)	(3)	(4)	(5)	(6)	(7)	(8)	(9)	(10)	(11)
NGC 1365	(R <sup>+</sup> )SB(rs <sub>+</sub> ,nr)bc	10.99	19.57	1.23	1613.3	201.1	88.5 (65 <sup>a</sup> )	55.4	94.9	1.15
NGC 1512	(RL <sup>-</sup> )SB(r,bl,nr)a	10.71	18.83	0.11	871.4	261.9	43.07	42.5	91.3	1.25
NGC 1672	(R <sup>+</sup> )SAB <sub>a</sub> (rs,nr)b	10.73	19.40	0.88	1319.2	134.3	-84.0	42.6	94.1	0.96
NGC 3627	SB <sub>a</sub> (s)b pec	10.83	11.32	0.58	717.9	173.1	-22.81	57.3	54.9	1.05

**Notes.** (1): Galaxy name. (2): MIR galaxy morphology (Buta et al. 2015). (3): Stellar mass (Leroy et al. 2021b). (4): Distance (Anand et al. 2021). (5): SFR (Leroy et al. 2021b). (6): Systemic velocity (Lang et al. 2020). (7): PA of the galaxy from CO kinematics, counterclockwise from the north (Lang et al. 2020). (8): PA of the bar measured using 3.6  $\mu\text{m}$  images (Salo et al. 2015). (9): Inclination (Lang et al. 2020). (10): Scale of PHANGS-MUSE data (Emsellem et al. 2022). (11): FWHM of the Gaussian PSF of the homogenized, convolved, and optimized (“copt”) PHANG-MUSE mosaic (Emsellem et al. 2022).

<sup>a</sup> the PA of the bar dust lane of NGC 1365. As it is different from the PA of the stellar bar for NGC 1365, we rotate NGC 1365 with the PA of the bar dust lane when we obtain the velocity gradient map.

stem from various samples of different bar evolutionary phases (e.g., Verley et al. 2007; Fraser-McKelvie et al. 2020).

Several mechanisms have been introduced to explain the suppression of SF in the bar region. First, bar-driven high shear prevents SF (e.g., Tubbs 1982; Athanassoula 1992; Zurita et al. 2004; Kim et al. 2012a; Emsellem et al. 2015; Renaud et al. 2015). Studies using simulations find that shear may suppress the growth of gravitational instability to form stars. Second, cloud–cloud collisions have been found to affect SF (e.g., Stone 1970; Scoville et al. 1986). If the relative velocity of two colliding gas clouds is high, i.e., if the gas clouds enter into the dust lane with high velocity, then the SF can be suppressed (e.g., Tubbs 1982; Reynaud & Downes 1998; Fujimoto et al. 2014; Maeda et al. 2021). Third, all of the gas within the bar extent may already have been converted into stars, and thus, gas is depleted, and the current SF is low (Spinoso et al. 2017; James & Percival 2018). Fourth, the fraction of dense gas is related to SF and SFE (Solomon et al. 1992; Gao & Solomon 2004; Muraoka et al. 2009; Usero et al. 2015; Bigiel et al. 2016), and vigorous motions near the dust lane make it difficult for dense gas to survive and may only exist as diffuse gas in the bar region between the center and bar ends (e.g., Sorai et al. 2012; Muraoka et al. 2016; Yajima et al. 2019). Lastly, turbulence (Elmegreen & Scalo 2004; McKee & Ostriker 2007; Haywood et al. 2016; Khoperskov et al. 2018; Sun et al. 2020) and magnetic fields found in the dust lanes of the bar (Beck et al. 1999; Kim & Stone 2012b) may prevent molecular clouds from collapsing to form stars (Krumholz & Federrath 2019).

Extensive studies on NGC 1530, an archetypal barred galaxy, have been performed on kinematics. Reynaud & Downes (1998) argue that the SF in NGC 1530 is inhibited in dust lanes where shocks and shear are expected to be strong. Using Fabry–Pérot interferometry in  $H\alpha$  on NGC 1530, Zurita et al. (2004) present clear observational evidence that shear inhibits massive SF, whereas shocks act to enhance it.

Another aim of this paper is to examine whether the emission-line ratios are modified due to the bar-driven shocks and shear. Several studies show that shocks from stellar winds, stellar feedback, supernova explosions, and galactic outflows can change the optical emission-line ratios (e.g., [O III]/ $H\beta$ , [N II]/ $H\alpha$ , [S II]/ $H\alpha$ , and [O I]/ $H\alpha$ , Shull & McKee 1979; Calzetti et al. 2004; Hong et al. 2013; Ho et al. 2014). Shocks with velocities greater than  $110 \text{ km s}^{-1}$  can generate sufficient UV radiation for the complete ionization of H and He (Shull & McKee 1979). Depending on the shock velocity and

contribution of shock, emission-line ratios can change from the star-forming to the low-ionization nuclear emission-line region (LINER) in the Baldwin–Phillips–Terlevich (BPT) diagram (Figure 13 of Ho et al. 2014). Therefore, we examine the emission-line ratio of the bar-driven shocks and shear region in the BPT diagram in order to see whether bar-driven shocks and shear can change the gas properties.

The paper is organized as follows. We describe the data and the analysis in Section 2. We explain the methods to estimate the  $H\alpha$  velocity gradients to identify bar-driven shock and shear in Section 3. We quantify velocity jumps across the high-velocity gradients in Section 4. We investigate whether the bar-induced shocks and shear promote or prevent SF in Section 5. By examining the BPT map, we classify the ionizing source on each spaxel, and assess the impact of bar-driven shocks and shear on SF in Section 6. We conclude and summarize our results in Section 7.

## 2. Data

We make use of data products from the PHANGS-MUSE survey (Emsellem et al. 2022). We use the mosaicked data cubes and emission-line fluxes, gas, and stellar kinematics, which were convolved and optimized in terms of resolution (“copt”). The point-spread function (PSF) of these data has been homogenized spatially across the galaxy, and the seeing of the “copt” data of our sample spans from  $0''.96$ – $1''.25$ .  $H\alpha$  flux and kinematics of PHANGS-MUSE are obtained using pPXF (Cappellari & Emsellem 2004). The  $H\alpha$  emission line is fitted, treating it as an additional Gaussian function, while the stellar continuum is fitted simultaneously. The velocity and velocity dispersion for  $H\alpha$  and  $H\beta$  are tied together. Detailed descriptions can be found in Emsellem et al. (2022). The spectral resolution is  $\sim 50 \text{ km s}^{-1}$  at  $H\alpha$ . CO (2–1) emission-line flux and velocity maps are drawn from the PHANGS-ALMA survey (Leroy et al. 2021b).

The basic properties of our four sample galaxies are presented in Table 1. We present an optical image, maps of the  $H\alpha$  velocity, a galaxy rotation model from the  $H\alpha$  velocity, the difference between the  $H\alpha$  velocity and galaxy rotation model, the  $H\alpha$  intensity, the stellar velocity, and the difference between the  $H\alpha$  velocity and the stellar velocity for NGC 1365 in Figure 2 as an example. In order to model the galaxy rotation, we utilize 3D-BAROLO (Di Teodoro & Fraternali 2015), which is a tool for fitting 3D tilted-ring models to emission-line data cubes. The position angle (PA), inclination

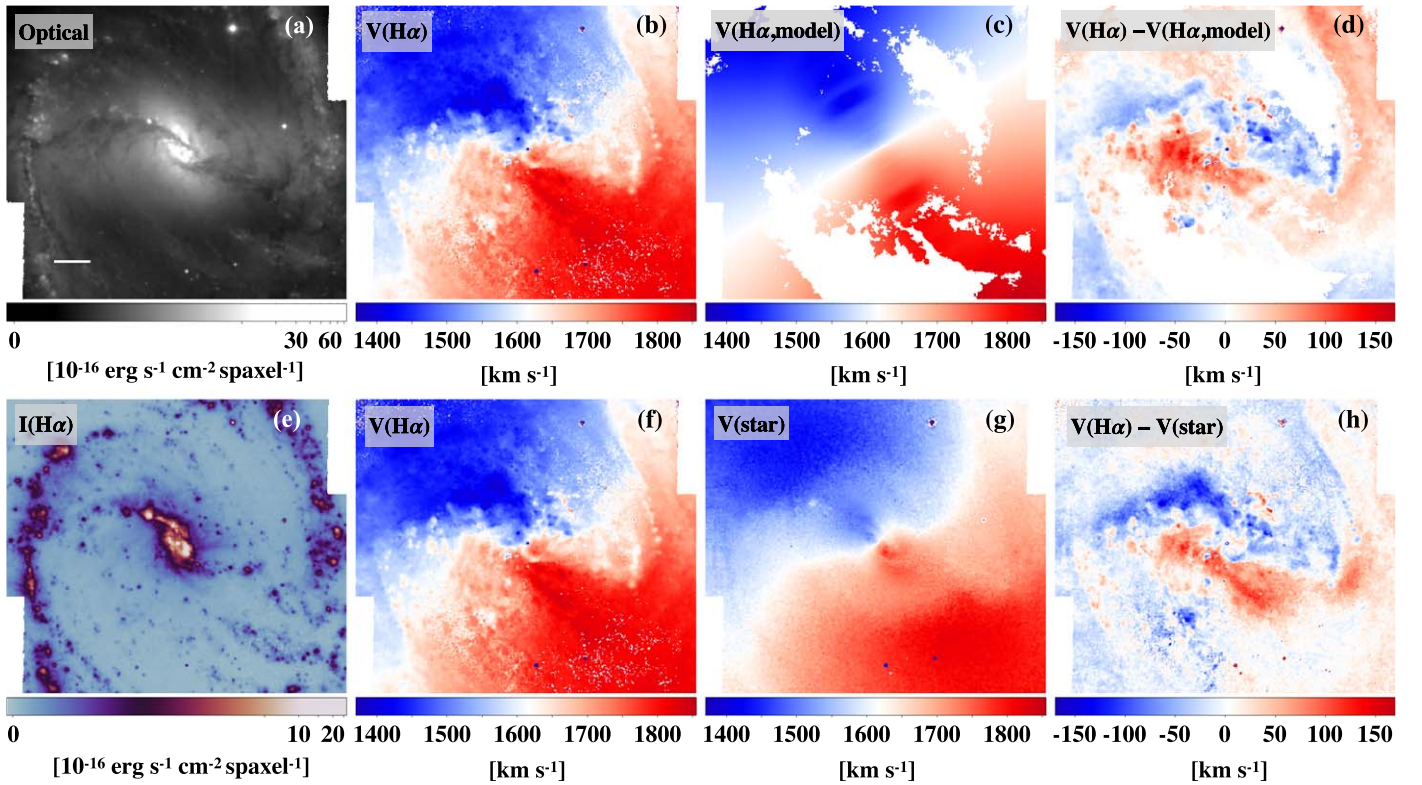


**Figure 2.** NGC 1365 (a): PHANGS-MUSE 5400  $\sim$  5600  $\text{\AA}$  summed image. North is up and east to the left. (b):  $\text{H}\alpha$  velocity field, ( $V_{\text{H}\alpha}$ ), (c):  $\text{H}\alpha$  velocity model obtained using 3D-BAROLO. White regions denote masked regions. (d):  $\text{H}\alpha$  residual velocity map, i.e., ( $V_{\text{H}\alpha} - V_{\text{H}\alpha, \text{model}}$ ), obtained by (b), (c), (e):  $\text{H}\alpha$  emission-line map, (f):  $\text{H}\alpha$  velocity field, ( $V_{\text{H}\alpha}$ ), (g): stellar velocity field,  $V_{\text{star}}$ , (h): velocity difference between  $\text{H}\alpha$  velocity map and stellar velocity map, ( $V_{\text{H}\alpha} - V_{\text{star}}$ ) obtained by (f) and (g).

of the galaxies, and center are fixed to the values from Table 2 of Lang et al. (2020) in running 3D-BAROLO. The velocity dispersion and scale height of the disk are fixed to  $8 \text{ km s}^{-1}$  and  $0''$ , respectively, which are the initial values implemented in 3D-BAROLO. An example of a rotation model is presented in Figure 2(c). We present velocity differences between the  $\text{H}\alpha$  velocity and the  $\text{H}\alpha$  rotation model in Figure 2(d), and the velocity differences between  $\text{H}\alpha$  velocity and stellar velocity maps in Figure 2(h).

### 3. Velocity Gradient

#### 3.1. Deriving Gas Velocity Gradient Maps

To explore bar-driven noncircular motions, it is necessary to remove the effect of circular motions. Noncircular motions can be measured in two ways. The first one is to obtain a galaxy rotation model and subtract it from the observed velocity field (i.e., the  $\text{H}\alpha$  velocity field in this study, Zurita et al. 2004). The second one is to utilize the differences between the gas and stellar velocity field, as gas and stars respond to the bar-driven gravitational forces differently. We use both methods to produce velocity gradient maps for NGC 1365 to explain the methodologies, compare them, and present results for other galaxies later in this section. We obtain the velocity gradient map first using the galaxy rotation model with the following steps.

1. From the  $\text{H}\alpha$  velocity map (Figure 2(b)), we subtract the  $\text{H}\alpha$  galaxy rotation model (Figure 2(c)) to obtain the  $\text{H}\alpha$  velocity residual map (Figure 2(d)).

2. We rotate the velocity residual map to align the bar horizontally using the PA of the bar presented in Table 1, and denote this map as  $V_{\text{res}}$ .
3. We move along the velocity residual map by 1 pixel ( $0''.2$ ,  $11 \sim 19 \text{ pc}$ , depending on the object) to the left ( $V_{\text{res}, -1\text{pix}}$ ) and to the right ( $V_{\text{res}, +1\text{pix}}$ ), and estimate the horizontal velocity gradient as

$$\nabla V_x = \frac{1}{2} (|V_{\text{res}} - V_{\text{res}, -1\text{pix}}| + |V_{\text{res}} - V_{\text{res}, +1\text{pix}}|). \quad (1)$$

4. We estimate the vertical velocity gradient ( $\nabla V_y$ ) similarly by moving 1 pixel up and down, perpendicular to the bar.
5. We add in quadrature both the horizontal ( $\nabla V_x$ ) and vertical ( $\nabla V_y$ ) velocity gradients to obtain the full velocity gradient,

$$\nabla V = \sqrt{\nabla V_x^2 + \nabla V_y^2}. \quad (2)$$

We plot the velocity gradient map for NGC 1365 in Figure 3(a). The velocity gradient is in the unit of  $\text{km s}^{-1} \text{ pc}^{-1}$ , and it is not corrected for galaxy inclination.<sup>17</sup> Zurita et al. (2004) show that velocity gradients perpendicular to the bar trace shear along the bar, while velocity gradients parallel to the bar trace shock along the bar. However, our sample galaxies show rather curved dust lanes. Thus, even velocity gradients perpendicular (parallel) to the bar may not perfectly represent

<sup>17</sup> As we do not intend to compare velocity gradients among different galaxies, velocity gradients are not corrected for inclination. The main conclusions we draw from Sections 5 and 6 do not change when correcting for inclination.

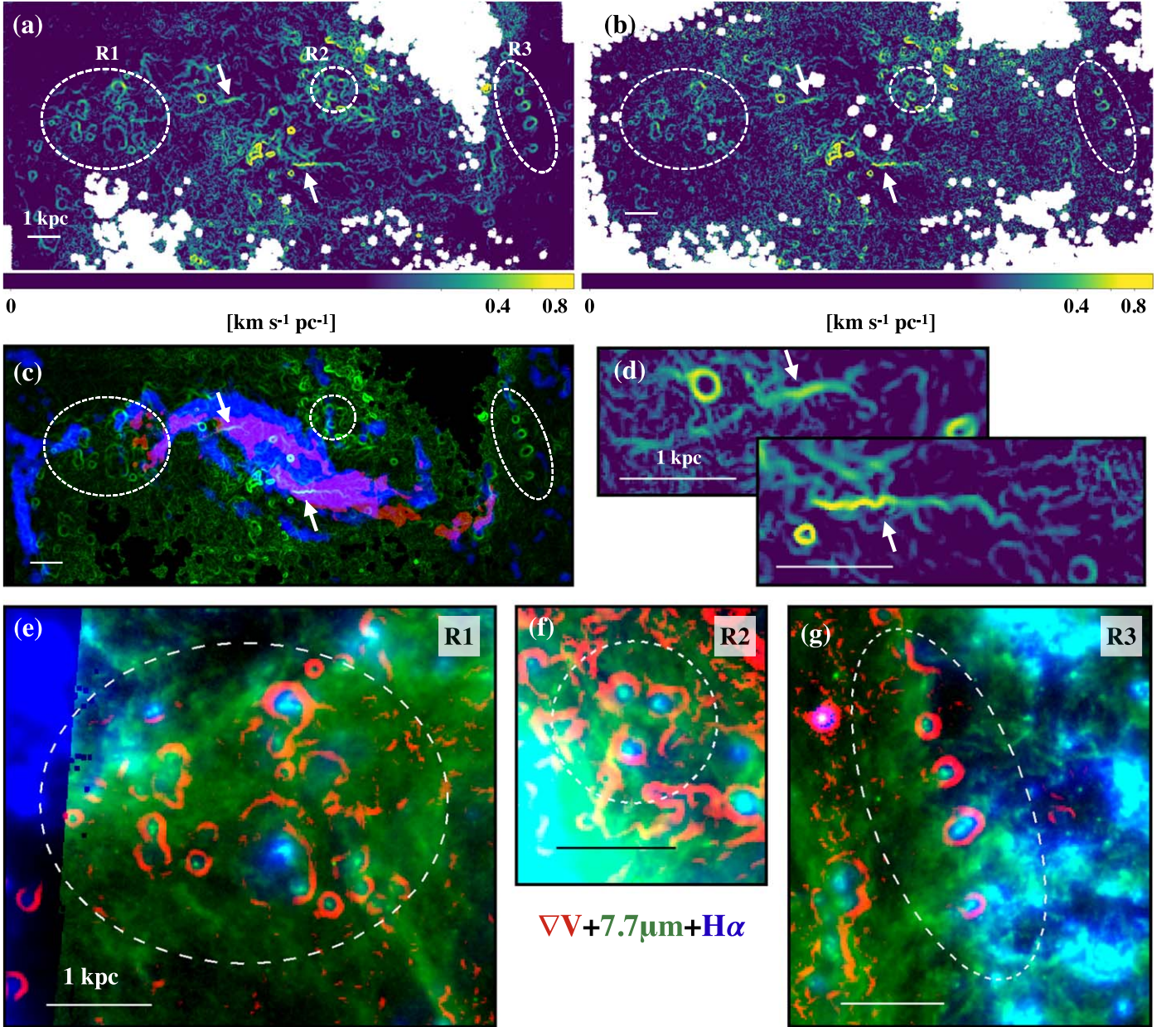


**Figure 3.** Velocity gradient map of NGC 1365. (a): velocity gradient map calculated using Equation (2) on the map of velocity residual of  $(V_{\text{H}\alpha} - V_{\text{H}\alpha, \text{model}})$ , in units of  $[\text{km s}^{-1} \text{pc}^{-1}]$ . The white horizontal line in the bottom left spans 1 kpc ( $10''/54$ ). (b): Velocity gradient map calculated using the map of  $(V_{\text{H}\alpha} - V_{\text{star}})$ . White arrows denote regions that are prominent in the velocity gradients map, which we infer to be driven by bar kinematics. White dashed ellipses indicate possible expanding shells around H II regions, superbubbles, or supernovae. (c): Velocity gradient map in green, CO  $J = 2-1$  line emission map from PHANGS-ALMA in blue, and the dust lane mask in red. The dust lane mask is made from the PHANGS-MUSE ancillary data that satisfy the ratio of Sloan Digital Sky Survey  $g$ -band flux over  $r$ -band flux is less than 0.8. (d): zoomed-in velocity gradient maps of regions pointed by two arrows. (e), (f), (g): zoomed-in red, green, and blue images of the white dashed ellipses in (a) and (b). Velocity gradients are displayed in red, JWST MIRI F770W images (Lee et al. 2023), which highlight PAH features at  $7.7 \mu\text{m}$ , are shown in green, and PHANGS-MUSE  $\text{H}\alpha$  emission-line maps are shown in blue. The shells in the figure have a radius in the range of  $\sim 50\text{--}350$  pc.

shear (shock). Therefore, we use  $\nabla V$  for further analysis. We present  $\nabla V_x$  and  $\nabla V_y$  in Appendix A for comparison.

Velocity gradients can also be estimated using the differences between the  $\text{H}\alpha$  and observed stellar velocities (Figure 2(h)). We calculate the  $V_{\text{H}\alpha} - V_{\text{star}}$  map and follow the same procedure from steps 2–5 to obtain the velocity gradient map of NGC 1365 (Figure 3(b)).

Comparing Figures 3(a) and (b), we find that the patterns are almost the same, while the one from subtracting the galaxy rotation model is more patchy, due to low signal-to-noise regions in estimating the galaxy rotation model. We found similar results for the other sample galaxies where galaxy rotation models are

radially smooth. However, when galaxy rotation models are not smooth, the resulting velocity gradient maps become bumpy and thus unsuitable for investigating the velocity gradients. Therefore, we opt to use the velocity gradient maps from  $V_{\text{H}\alpha} - V_{\text{star}}$  for further analysis, which is unaffected by the galaxy rotation model. In general, if a galaxy is dynamically hot (e.g., bulge-dominated galaxies), we cannot use stellar velocity fields to trace the galaxy's rotation because stars also reside outside the disk plane and are dynamically hotter than gas. However, as our sample of barred galaxies is relatively dynamically cold, Figure 3 shows that we can use the stellar velocity field to trace the galaxy rotation in order to obtain noncircular motions.

We also have tried to obtain the velocity gradient using CO from the PHANGS-ALMA data set. However, bar regions are not sufficiently detected or are patchy along and adjacent to the bar. Thus, it is not suitable to obtain the velocity gradient map over the full bar regions for our sample galaxies, although the spectral resolution is superb. We compare the velocity gradients of H $\alpha$  and CO in Appendix B, and conclude that we can use H $\alpha$  velocity gradients to trace molecular gas velocity gradients for our sample galaxies.

### 3.2. Two Different Types of Velocity Gradients

The velocity gradient map tells us where the velocity changes abruptly. As we add vertical and horizontal components in quadrature, it shows velocity change in both directions. Figure 3 shows that there are various shapes of enhanced velocity gradient regions, which can be categorized into two groups. First, along the bar dust lanes, there are enhanced velocity gradients that are extended more than 1 kpc, as indicated with white arrows in Figures 3(a) and (b). These are directly connected to the gas inflow along the bar. Therefore, we claim that these velocity gradients are produced by bar-driven shocks and shear.

Second, there are circular or arc-shaped enhanced velocity gradients that are a few hundred parsecs in radius, which are not related to the bar but are spread throughout the galaxy (see the white dashed ellipses in Figure 3). The shape of the regions with enhanced velocity gradients suggests they are expanding. Such shapes of high-velocity gradients are especially numerous in NGC 1365. We find that H $\alpha$  sources and PAH emissions at  $7.7 \mu\text{m}$  are located at the center of these circles and arcs (see Figure 3). Thus, we infer that these might be due to the expanding shells from H II regions ionized by young stars or stellar associations (Relaño & Beckman 2005; Bresolin et al. 2020) or due to H II regions that are moving relative to the surroundings. Also, supernova remnants, superbubbles (Watkins et al. 2023), or prestellar compression shocks may well produce such high-velocity gradients. These velocity gradients are not artificially created by the procedures we followed. The velocity difference in these regions can even be seen directly in the H $\alpha$  velocity map and  $V_{\text{H}\alpha} - V_{\text{star}}$  in Figures 2(b) and (h). We will study these velocity gradients of expanding regions in more detail in a future paper, while in this work, we focus on the first type of high-velocity gradients and examine whether the bar-driven shocks and shear inhibit or promote SF.

### 3.3. Velocity Gradients Due to Bar-driven Gas Inflow

Velocity gradient maps for our sample galaxies are presented in Figure 4, along with optical, H $\alpha$ , and CO images. In deriving velocity gradient maps, we applied an amplitude-over-noise ratio of H $\alpha$  greater than 3. We exclude regions where the H $\alpha$  velocity errors ( $\delta V_{\text{H}\alpha}(x, y)$ ) are high in the velocity gradient map as follows. We mask out pixels where  $\delta V_{\text{H}\alpha}(x, y) > \langle \delta V_{\text{H}\alpha} \rangle + C \times \sigma(\delta V_{\text{H}\alpha})$ , where  $\langle \delta V_{\text{H}\alpha} \rangle$  is the average of H $\alpha$  velocity errors and  $\sigma(\delta V_{\text{H}\alpha})$  is the standard deviation of  $\delta V_{\text{H}\alpha}$  for each galaxy. Constant  $C$  is set to 0.2 for NGC 1365 and NGC 3627, while  $C$  is empirically set to  $-0.05$  for NGC 1512 and NGC 1672 to avoid spurious signals around the bar to produce a reliable velocity gradient map. The PHANGS-MUSE data sets are Voronoi binned to a target signal-to-noise ratio  $S/N = 35$  in the continuum range of  $5300\text{--}5500 \text{ \AA}$ . Therefore, regions with low signals have a large bin size. We

found that for some of those bins, the differences between H $\alpha$  and stellar velocity ( $V_{\text{H}\alpha} - V_{\text{star}}$ ) are artificially large, especially at the edge of those bins due to binning. We empirically find that those pixels can be removed if we remove pixels that have stellar velocity errors greater than the median of stellar velocity errors of each galaxy.

Enhanced velocity gradients clearly show up along the bar dust lanes, and they extend out for a considerable length, almost covering the whole bar except for NGC 1365. The velocity gradients of the bar region in NGC 1365 range between  $0.1$  and  $1.0 \text{ km s}^{-1} \text{ pc}^{-1}$ . This is consistent with the study of Zurita et al. (2004), who find velocity gradients up to  $0.35 \text{ km s}^{-1} \text{ pc}^{-1}$  for NGC 1530 and also consistent with the study of Kim et al. (2012a), who find  $1\text{--}3 \text{ km s}^{-1} \text{ pc}^{-1}$  of shear across the bar dust lane from numerical simulations. Our results should be considered as a lower limit of the velocity gradient because of the smoothing effect due to the spatial resolution ( $0''.2 \text{ pixel}^{-1}$ ) and spectral resolution ( $2.6 \text{ \AA}$ , corresponds to  $50 \text{ km s}^{-1}$  at H $\alpha$ ). Detailed notes on each object are available in Appendix D.

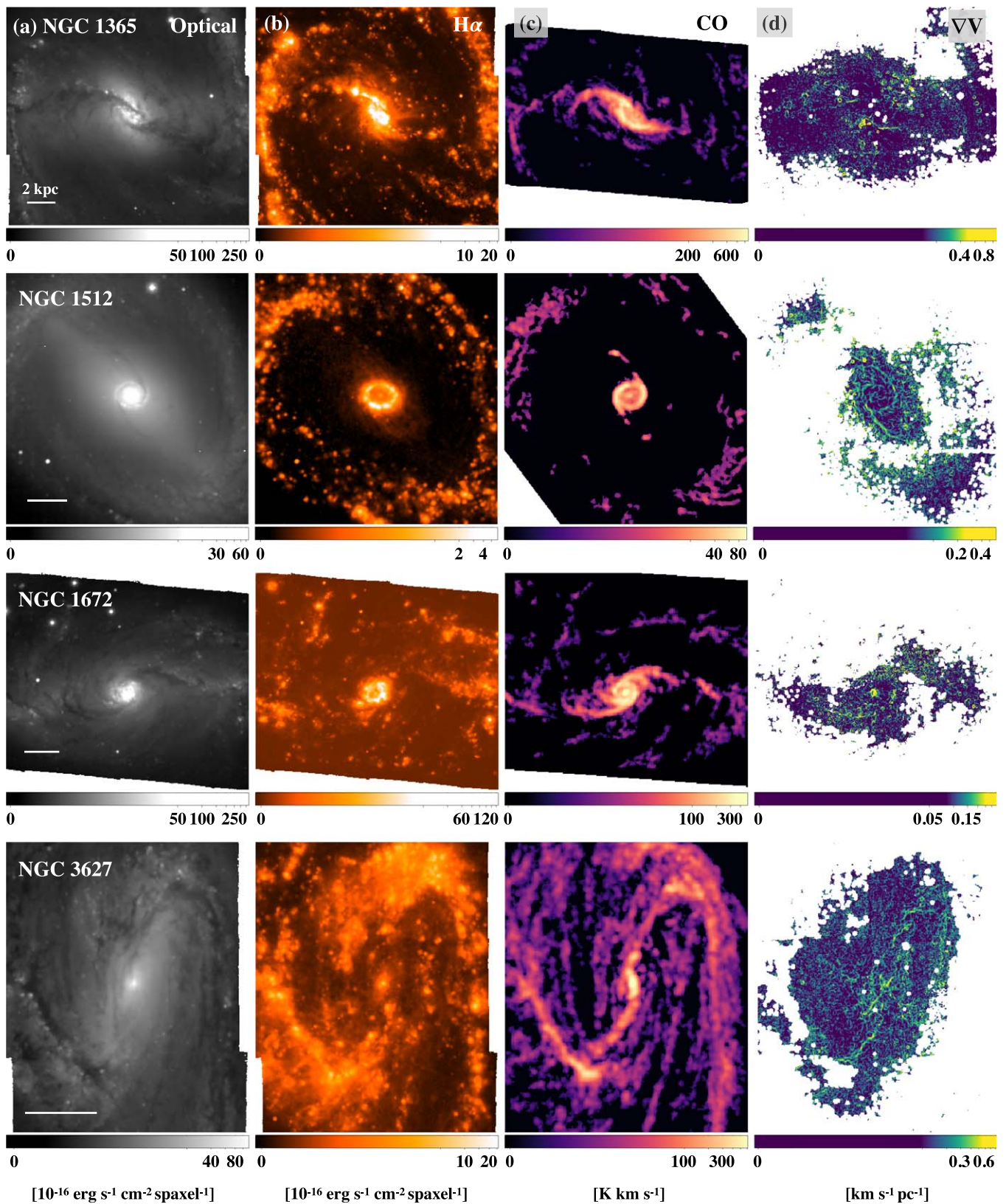
### 3.4. Comparison to the CO Map

Figure 4 shows that the velocity gradients are pronounced along the bars in all samples of galaxies. But exactly where are the velocity gradients enhanced? Previous studies have found that the velocity gradients coincide with the dust lane, i.e., on the leading side of the bar (see, e.g., Zurita et al. 2004 and Feng et al. 2022 for studies on NGC 1530 and M31, respectively).

We plot CO emission-line contours on top of the velocity gradient map in Figure 5 for comparison. We find that velocity gradients are enhanced either along the bar dust lane inferred from the CO distribution or slightly offset to the edge of the bar dust lane. In NGC 1365, the southern part of the enhanced velocity gradients is located right next to the brightest contour of the CO emission along the bar dust lane. We find that in NGC 1512, enhanced velocity gradients coincide with the CO emission detected along the bar dust lane, which can be seen in the optical image. However, in NGC 1672 and NGC 3627, velocity gradients are slightly offset toward the peak of the CO emission. Velocity gradients are enhanced on the leading side of the bar in NGC 1672 and in the southern part of NGC 3627. Interestingly, in the northern part of the bar in NGC 3627, it is the opposite. Details on NGC 3627 are in Appendix D. In summary, the locations of enhanced velocity gradient regions either coincide with the peak of the CO emissions or are slightly offset to them, depending on the objects.

## 4. Velocity Jumps

We quantify how much velocity jump occurs in the regions where strong bar-driven shocks and shear are expected for our sample galaxies. In order to estimate velocity jumps, we place pseudo-slits perpendicular to the regions of the high-velocity gradient in the bar region. Figure 6 shows the velocity changes along the slits in selected regions for NGC 1365. We find that the velocity jump exceeds  $100 \text{ km s}^{-1}$  within  $2''$  ( $190 \text{ pc}$ ) in both H $\alpha$  and CO in slits 1 and 3. Within  $5''$  ( $475 \text{ pc}$ ), the velocity of CO changes up to  $200 \text{ km s}^{-1}$ , and that of H $\alpha$  changes up to  $150 \text{ km s}^{-1}$  in slit 1. The inclination of NGC 1365 is estimated to be  $55^\circ.4$  (Lang et al. 2020). Thus, the velocity jump would become even higher ( $\times 1.2$  for NGC



**Figure 4.** (a): Optical image from PHANGS-MUSE,  $5400 \sim 5600 \text{ \AA}$  summed image. The white line on the bottom left covers 2 kpc for each galaxy. North is up and east to the left. (b): PHANGS-MUSE  $\text{H}\alpha$  flux map. (c):  $\text{CO } J = 2-1$  line emission map from PHANGS-ALMA, and (d): velocity gradient map calculated using  $(V_{\text{H}\alpha} - V_{\text{star}})$ . Velocity gradients are not corrected for inclinations.

1365) if we correct for inclination. We note that these velocity jumps are measured directly from the velocity map, and therefore are not model dependent.

While the gaseous velocity jumps are prominent, the stellar velocity jumps are not as pronounced in these regions. The degree of velocity jumps may be different between gas and

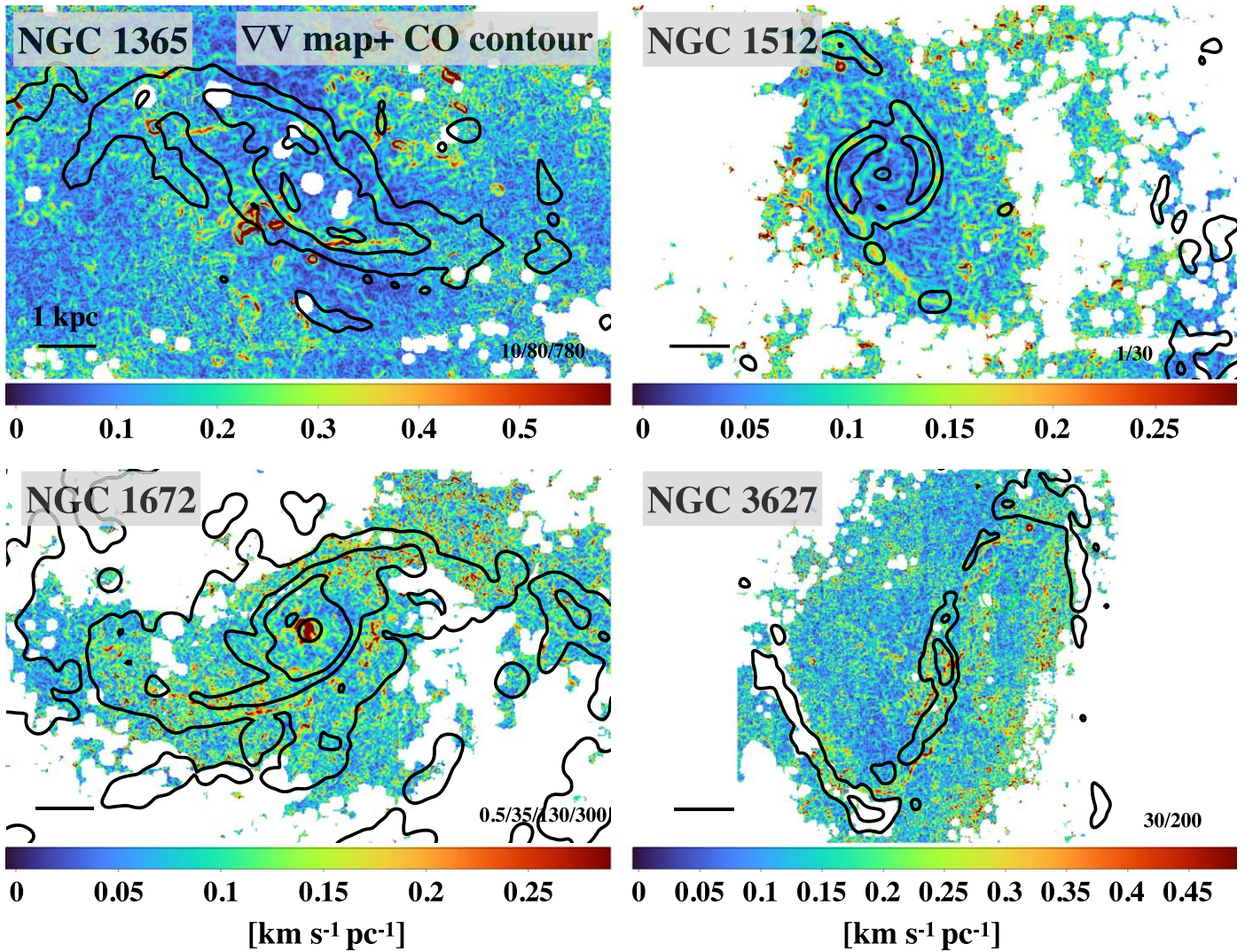


**Figure 5.** Velocity gradient map superimposed with contours that correspond to the emission-line flux of CO (2–1) from the PHANGS–ALMA survey. Numbers in the bottom right of each panel correspond to the CO contour levels in  $[\text{K km s}^{-1}]$ . The black line on the bottom left covers 1 kpc for each object.

stars because they respond differently to the gravitational forces of the bar. Gas is dynamically cold and thus highly responsive to the changes in the gravitational potentials it feels as it orbits in the disk. In addition, gas is collisional and thus easily influenced by shear and shocks, and therefore loses angular momentum more easily, which leads to stronger noncircular motions. However, stars are generally not affected by shocks, and stars making up bars are in more stable orbits, which leads to milder velocity jumps.

Components of galactic rotation are included in the velocity map and thus in these velocity jumps. Therefore, to exclude the effects of circular motions from galaxy rotation, we subtract the galaxy rotation model from the  $\text{H}\alpha$  velocity map. Then, we assess the velocity jump in the bottom right panel of Figure 6. In fitting galaxy kinematics using 3D-BAROLO, PAs and inclinations can be fixed or freely modeled ring by ring. We present both results. Even after the circular motions are removed, we still find the velocity changes reaching  $140 \text{ km s}^{-1}$  ( $170 \text{ km s}^{-1}$  after deprojection) within  $2''$  (190 pc) in slit 3 and  $90 \text{ km s}^{-1}$  ( $110 \text{ km s}^{-1}$  after deprojection) within  $4''$  (380 pc) in slit 1 for NGC 1365. Velocity jumps and the position of pseudo-slits of other sample galaxies are presented in Appendix C. Velocity jumps of other sample galaxies after removal of the galaxy

rotation span from  $50\text{--}80 \text{ km s}^{-1}$  ( $75\text{--}95 \text{ km s}^{-1}$  after deprojection) within  $2''$  and  $\text{H}\alpha$  velocity jumps are more pronounced compared to stellar velocity jumps as in NGC 1365.

Velocity jumps reaching  $\sim 100\text{--}150 \text{ km s}^{-1}$  have been found using  $\text{H}\alpha$ ,  $[\text{N II}]$ ,  $[\text{S II}]$ ,  $\text{H I}$ , and CO (Pence & Blackman 1984; Reynaud & Downes 1998; Laine et al. 1999; Mundell & Shone 1999; Weiner et al. 2001; Zurita et al. 2004), and even up to  $200 \text{ km s}^{-1}$  (Zánmar Sánchez et al. 2008; Feng et al. 2022). Thus, our results are comparable to previous observational studies on the other objects. With idealized hydrodynamic simulations, Kim et al. (2012a) show that the velocity along the slit direction changes abruptly by up to  $100 \text{ km s}^{-1}$  within 100 pc, while the velocity perpendicular to the slit direction jumps up to  $200 \text{ km s}^{-1}$  within 100 pc in their Figure 8. It is not straightforward to directly compare the values of velocity jump from simulations with our observational data analysis because we only measure the line-of-sight velocity. Nevertheless, overall results are still comparable. If we know the bar pattern speed and the inclination of the galaxy, we can derive the gas velocity vector (e.g., Sormani et al. 2023) by assuming that the gas velocity vector in the bar lanes is parallel to the lane, but this is beyond the scope of this paper.



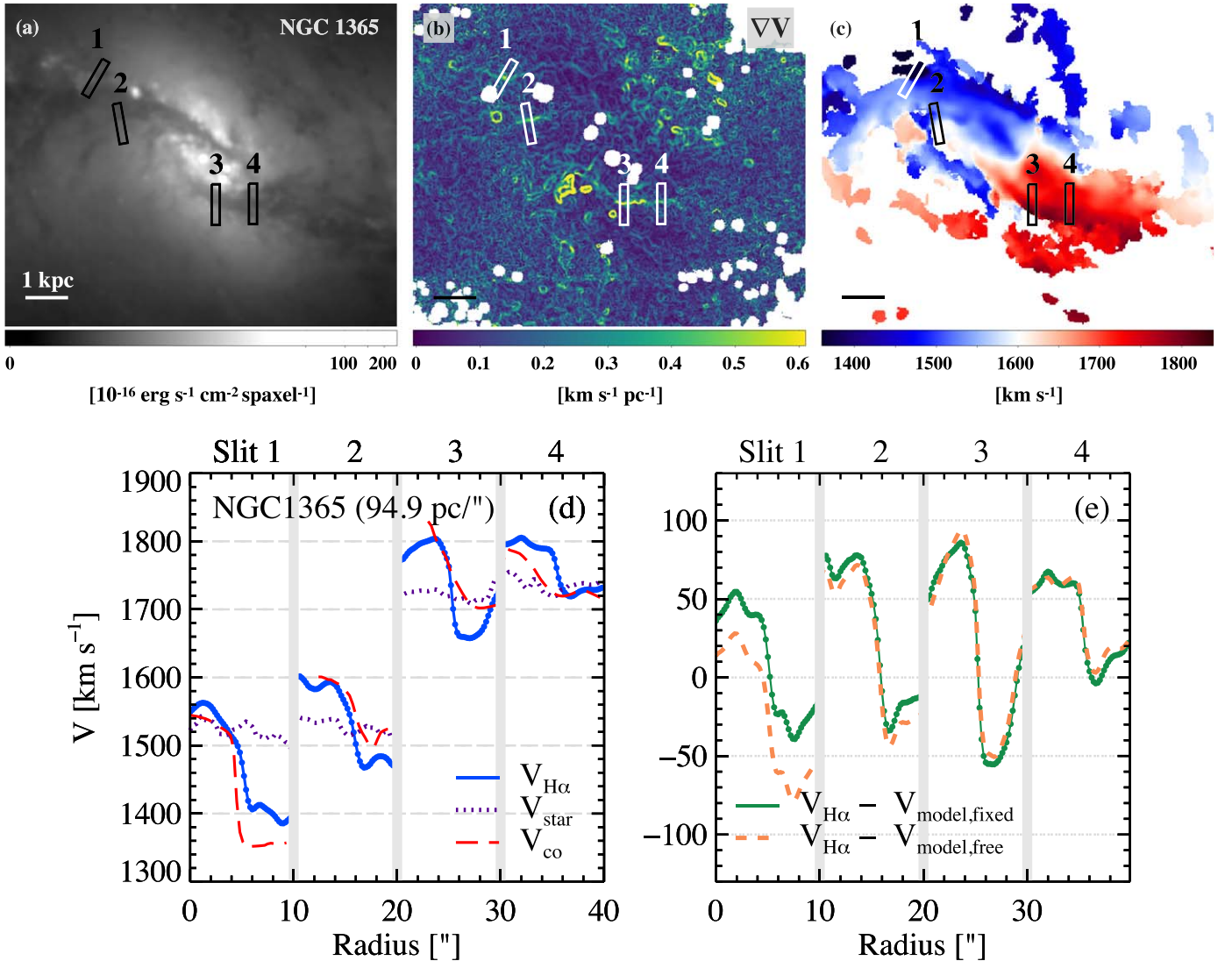


**Figure 6.** Velocity jumps in high-velocity gradient regions of NGC 1365. Four pseudo-slits ( $0''.6 \times 10''$ ) are put perpendicular to the high-velocity gradient segments as in the upper panels of the figure. (a): optical image of NGC 1365, (b): velocity gradients, (c): CO (2–1) velocity, (d) velocity jumps from south to north (upward) along the slit of H $\alpha$  (blue solid line), CO (red dashed line, if available), and stellar velocity (purple dotted line), (e) velocity jumps after removal of the galaxy rotation model. Two cases of galaxy rotation models are obtained with 3D-BAROLO, where PAs and inclinations are fixed (green solid line) and set to free (orange dashed line) for each ring. Velocity jumps for other sample galaxies are presented in Appendix C.

### 5. Impact of Shear and Shock on SF

In this section, we examine the impact of bar-driven shear and shock on SF, which can be traced approximately by velocity gradients and H $\alpha$  emission, respectively. With this aim, we compare the velocity gradients with H $\alpha$  emission-line maps spatially. Figure 7 shows an extinction-corrected H $\alpha$  emission-line map superimposed with the velocity gradient contours. To correct for extinction, we use the flux ratio of two emission lines, H $\alpha$ /H $\beta$  (Balmer decrement; e.g., Berman 1936; Groves et al. 2012). We assume the value of the intrinsic H $\alpha$ /H $\beta$  to be 2.86, corresponding to a temperature  $T = 10^4$  K and an electron density  $n_e = 10^2 \text{ cm}^{-3}$  for Case B recombination (Baker & Menzel 1938). Overall, bright H $\alpha$  sources are rarely found in high-velocity gradient regions along the bar. In particular, SF in NGC 1512 is concentrated in the nuclear ring and the inner ring that encircles the bar, and bright H $\alpha$  sources are rare inside the ring that encompasses the bar. In NGC 3627, there are many star-forming regions along the spiral and

interarm regions. Interestingly, high-velocity gradients are avoiding bright star-forming regions. Overall, bright SF knots are not found on the enhanced velocity gradient regions.

Then, we examine whether there is an anticorrelation between star-forming sites and regions of strong shear and shock in a quantitative approach. We plot the SFR surface density and velocity gradients in Figure 8. Each point corresponds to a spaxel. To focus on the shear and shock regions that are directly connected to the gas inflow along the bar, we select the bar regions outside the nuclear region and inside the bar ends, and plot the selected regions in color according to each spaxel’s molecular gas surface density in Figure 8. Nuclear regions, bar ends, outside the bar regions, and regions with no PHANGS-ALMA CO (2–1) detection are plotted in gray. We use the environmental masks from Querejeta et al. (2021) to define the bar, bar ends, and nuclear regions.

The SFR is calculated based on H $\alpha$  luminosity. H $\alpha$  traces recent SF as 90% of the H $\alpha$  emission comes from stellar

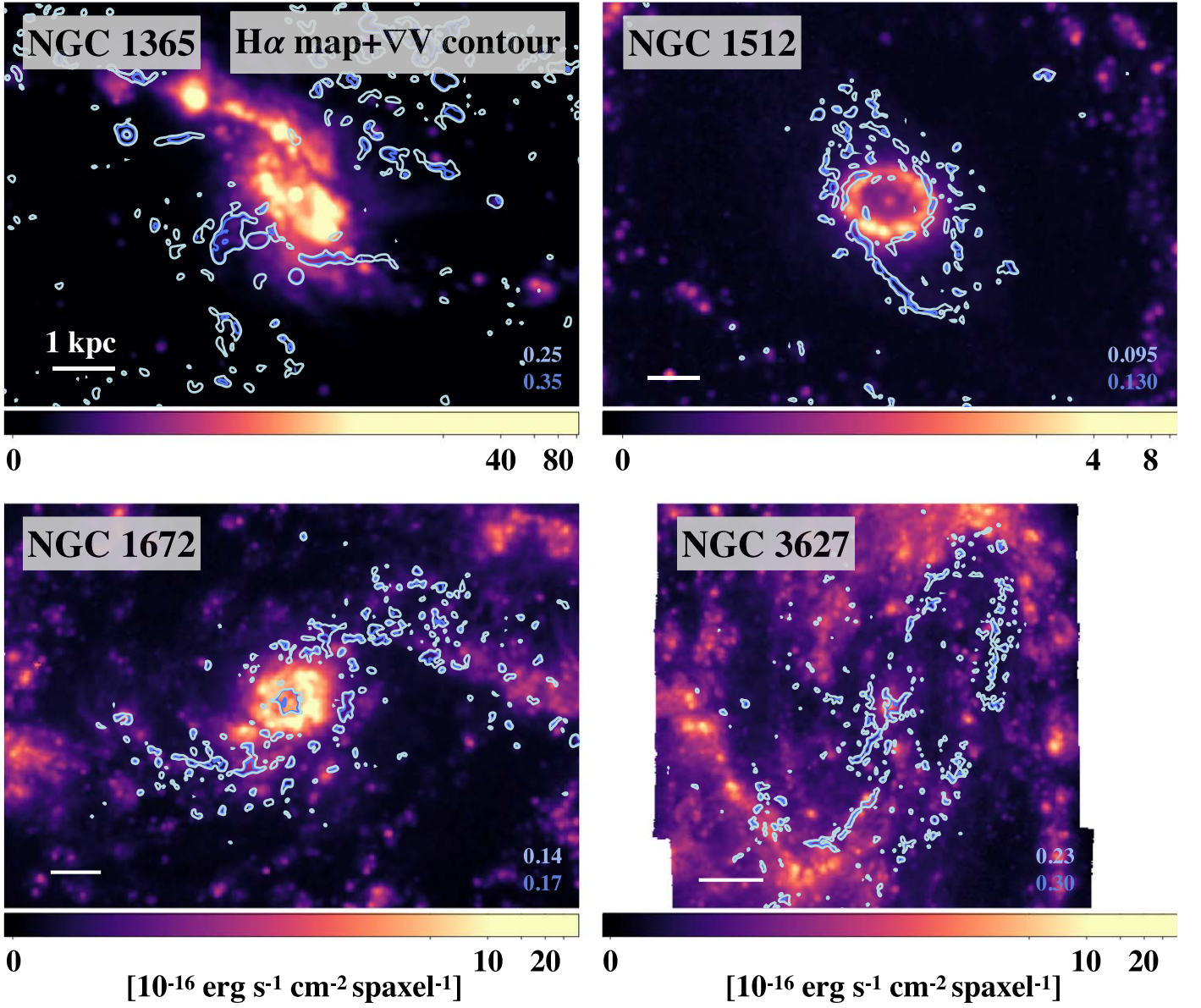


**Figure 7.** Extinction-corrected H $\alpha$  emission-line maps overlaid with the velocity gradient contours. The white line on the bottom of each panel spans 1 kpc. The two numbers on the bottom right in each panel correspond to the velocity gradient contour levels in  $[\text{km s}^{-1} \text{ pc}^{-1}]$ . Darker blue shades represent higher velocity gradients.

populations younger than 10 Myr (Kennicutt & Evans 2012). Although the SFR can be better estimated with hybrid estimators in combination with H $\alpha$ , mid-infrared (MIR), and/or far-UV data, it has been shown that once stellar continuum absorption and dust attenuation are properly corrected, there is a good correlation between the SFR derived from H $\alpha$  and the SFR derived from H $\alpha$ , UV, and MIR data (Catalán-Torrecilla et al. 2015, see also Belfiore et al. 2023). Furthermore, to conserve the resolution of the H $\alpha$  velocity gradients, we use the SFR derived from H $\alpha$  luminosity in this study.

We estimate the SFR using the following relation (Calzetti et al. 2007; Kennicutt & Evans 2012):

$$\text{SFR} [M_{\odot} \text{ yr}^{-1}] = 5.3 \times 10^{42} L(\text{H}\alpha)_{\text{corr}} [\text{erg s}^{-1}], \quad (3)$$

where  $L(\text{H}\alpha)_{\text{corr}}$  is the extinction-corrected H $\alpha$  luminosity. The molecular mass surface density can be estimated using CO(2–1)

as

$$\Sigma_{\text{mol}} = \alpha_{\text{CO}}^{1-0} R_{21}^{-1} I_{\text{CO}(2-1)} \cos i, \quad (4)$$

where  $\alpha_{\text{CO}}^{1-0}$  is the CO(1–0) conversion factor,  $R_{21}^{-1}$  the CO(2–1)–to–CO(1–0) line ratio, and  $i$  the inclination of a galaxy. We use  $\alpha_{\text{CO}}^{1-0}$  of the standard Milky Way ( $4.35 [M_{\odot} \text{ pc}^{-2} (\text{K km s}^{-1})^{-1}]$ , Bolatto et al. 2013), and we use  $R_{21}^{-1} = 0.65$  (Leroy et al. 2013; den Brok et al. 2021).

If shear and shocks prevent SF, there should be an anticorrelation between the SFR surface density and the velocity gradients, i.e., the SFR surface density should decrease with the velocity gradients. However, Figure 8 shows that while the upper envelope of the SFR surface density–velocity gradient decreases, data points fill the area below the upper envelope. In low-velocity gradient regions, there are regions of diverse values of SFR surface density. However, as the velocity gradient increases, the upper envelope of SFR surface density decreases. If we combine it with molecular gas density, this

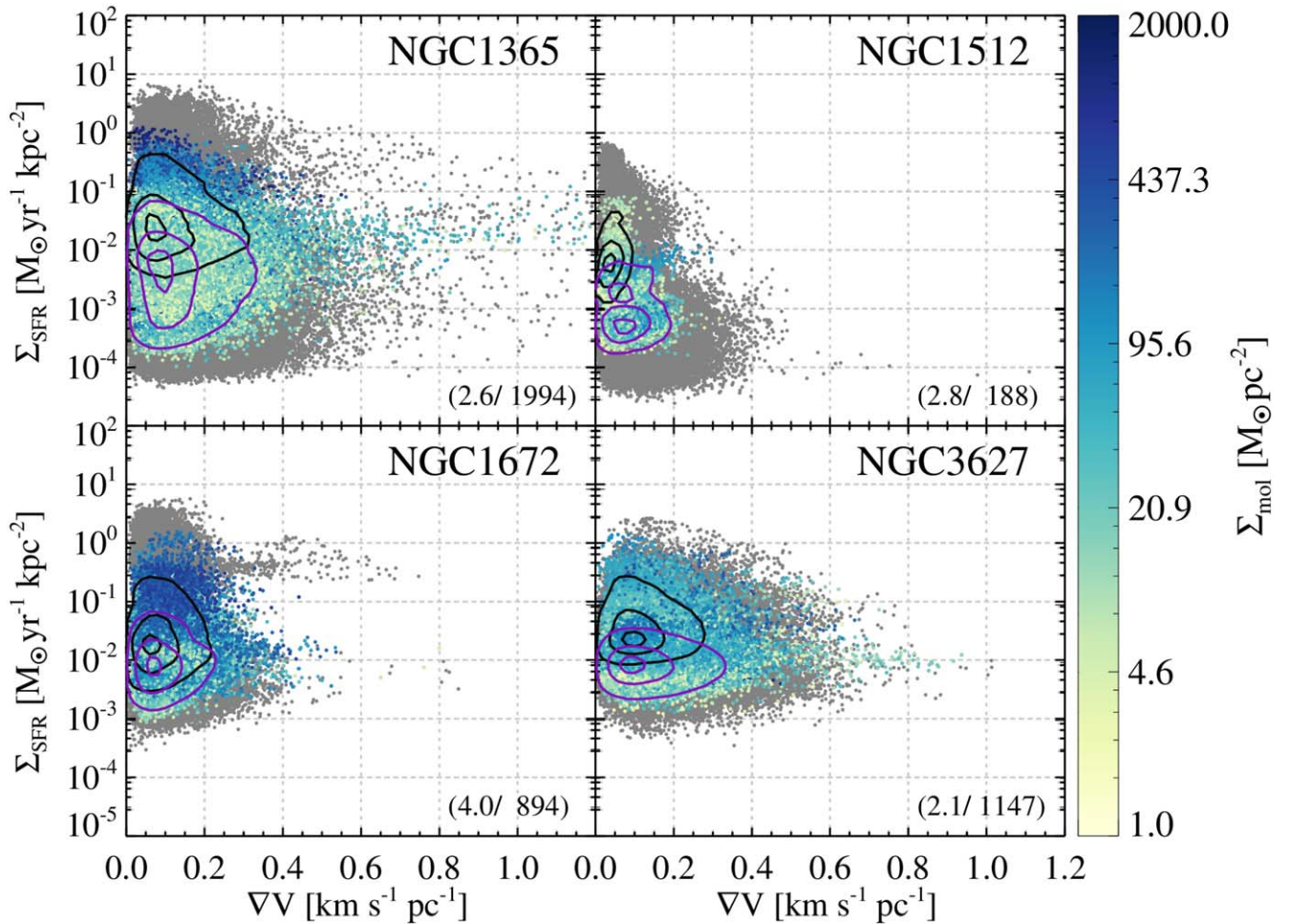


**Figure 8.** SFR surface density and velocity gradients. Each point corresponds to a spaxel. Bar regions defined by Querejeta et al. (2021) (excluding nuclear region and bar ends) are color-coded according to molecular surface density. Spaxels outside the bar regions and no PHANGS-ALMA CO(2–1) detection are plotted in gray. We show the minimum and maximum of the molecular gas surface densities of bar regions in parenthesis for each galaxy. Black contours contain 10%, 50%, and 90% of star-forming spaxels in the bar region, where the bar ends and nuclear regions are excluded. Purple contours include 10%, 50%, and 90% of LINER, Seyfert, and composite spaxels in the bar region classified by the BPT diagnostics, which are detailed in Section 6.

distribution becomes clear to understand. In low-velocity gradients, i.e., low shear and shock, regions with high molecular gas density regions show active SF. In the high shear/shock region, active SF is rare. Exceptions are the nuclear regions of NGC 1365 and NGC 1672 where they protrude horizontally in the SFR surface density–velocity gradients diagram. Our results imply that SF is hindered in bar-driven shear and shocks. This is consistent with previous studies (Reynaud & Downes 1998; Zurita et al. 2004), who conclude that steep velocity gradients prevent molecular gas clouds from condensing to form stars.

Our results are in line with the study of Emsellem et al. (2015), who find a notable correlation between the regions of newly formed stars and the location of high-density gas clumps with low shear but not with high shear using hydrodynamical simulations of a Milky Way–like galaxy. In the next section, we revisit the impact of bar-driven shear and shock on SF using the BPT classification.

## 6. Changes to Emission-line Ratios Due to Bar-driven Shear and Shocks: BPT Diagrams

### 6.1. BPT Map

We examine whether shear and shocks driven by bars lead to any change in the ionized gas properties by inspecting emission-line ratio diagnostic diagrams.

Dominant ionizing sources of gas can be separated using the BPT diagram (Baldwin et al. 1981; Veilleux & Osterbrock 1987; Kewley et al. 2001; Kauffmann et al. 2003). A theoretical maximum starburst line (Kewley et al. 2001, solid line in Figure 9) is defined by the upper limit of the theoretical pure stellar photoionization model. Points above this line are likely to be dominated by gas ionized by an AGN or shock. Points below the dotted line in Figure 9 (Kauffmann et al. 2003) represent regions where the emissions come from pure SF. The regions between the dotted line and solid line indicate that gas is ionized by both SF and AGN and thus is named *composite*. The dashed line (Cid Fernandes et al. 2011) divides Seyfert and LINER. We plot the BPT diagram for NGC 1365 in Figure 9. Each point denotes a spaxel of the galaxy. All the spaxels that satisfy the amplitude-over-noise ratio of emission lines greater than 5 are plotted. Blue points represent emissions from star-forming regions, and green ones denote composite spectra. Orange to red points correspond to Seyfert, and magenta points represent LINER. Points that are in close proximity to the maximum starburst line are plotted in lighter shades, whereas points distant from the maximum starburst line are denoted with darker shades. The corresponding maps for all galaxies in the sample are presented in Figure 10 with the same color coding as in Figure 9.

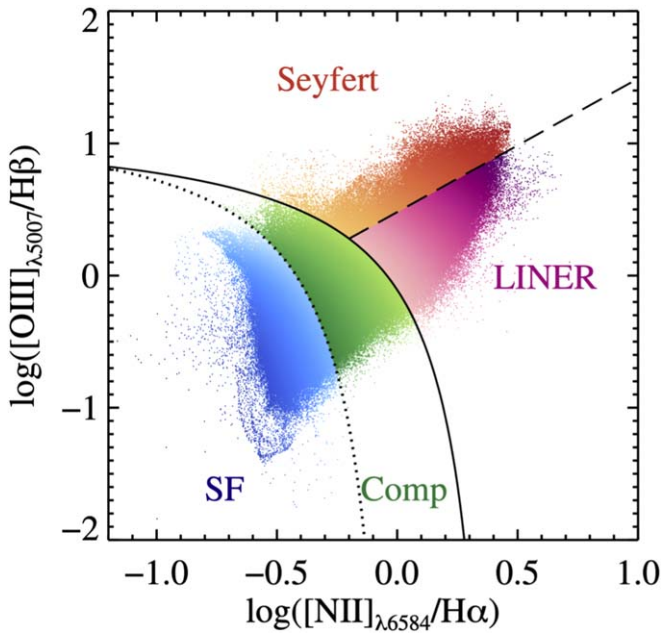


**Figure 9.** BPT diagram of NGC 1365. The solid line indicates the theoretical maximum starburst line (Kewley et al. 2001), the dotted line marks the limit of pure SF (Kauffmann et al. 2003), and the dashed line divides Seyfert and LINER (Cid Fernandes et al. 2011). Blue points denote emissions from SF regions, green points represent emissions from composite, both from SF and AGN, red to orange points stand for emissions from Seyfert, and magenta points correspond to emissions from LINER. Points become darker as they are farther away from the theoretical maximum starburst line (solid line).

NGC 1365 displays a biconical outflow (e.g., Phillips et al. 1983; Jorsater et al. 1984; Venturi et al. 2018; Gao et al. 2021). Within that outflow region, emission-line ratios are located in either the Seyfert or LINER area in the BPT diagram. Bar-driven high-velocity gradient regions are mostly composite, LINER, or Seyfert. The region marked by the yellow arrow in Figure 10 shows a remarkably sharp change compared to adjacent regions, from star-forming to composite and Seyfert type. However, in the other bar-driven high-velocity gradient regions, the ionizing sources seem to be contaminated by the outflow. Inside the bar radius of NGC 1512, the sources of ionization in most regions are LINER, and it also applies to strong shear regions driven by the bar. For NGC 1672, high shocks and shear regions are not preferentially occupied by any types of ionizing sources. In NGC 3627, the northern part of the high shear regions is mostly of composite or Seyfert type. However, the southern part of the high-shear regions shows either SF or a composite.

In the previous section, we plotted the velocity gradients and the SFR surface density in Figure 8. It contains all the spaxels of SF, LINER, composite, and AGN. If we only consider SF spaxels (black contours in Figure 8), the mean SFR surface density is approximately five times higher on average compared to the spaxels of composite, LINER, and Seyfert (purple contours in Figure 8). SF spaxels span a slightly narrow range of velocity gradients with a lower ( $\sim 20\%$  on average) mean value.

### 6.2. SF Classified with BPT Diagnostics

In order to reexamine whether the SF is inhibited in high shear/shock regions, we classify the ionizing sources using the

BPT diagnostics and compare them with those of low shear/shock regions in the bar, and all the other regions of the galaxy in Figure 11. Nuclear regions and bar ends are excluded in this *bar* region, as they exhibit active SF and shear and shocks, due to bar-driven gas inflow not being strong there. We define the high-velocity gradient regions in the bar (H) as those with velocity gradients greater than the upper 5th percentile in the bar for each galaxy, and define the low-velocity gradient regions in the bar (L) so that their velocity gradients are less than the upper 5th percentile. We also define the interbar (IB) region, outside the bar but still within the bar radius. We find that the fraction of the SF group in high-velocity gradient regions in the bar (H in Figure 11) is lower than that of low-velocity gradient regions in the bar (L) and all the other regions of the galaxy (A). The majority of high-velocity gradient regions exhibit composite or LINER. The fraction of the SF group in high-velocity gradient regions of the bar spans  $\sim 2\%$ – $40\%$ . This implies that SF is inhibited in high-velocity gradient regions in the bar, which is in line with our results from the previous section that bar-driven shear/shock hinders SF.

By analyzing 240 barred galaxies with MaNGA, Krishnarao et al. (2020) find that ionized gas is generally classified as LINER-like within the bars, composite in the IB regions, while ionized gas from SF is located either at the center and/or outside the bar radius. Figure 11 also shows that in the IB, the majority of spaxels are either composite or LINER, which is consistent with the results of Krishnarao et al. (2020). Except for NGC 1672, our sample galaxies fit well into their picture in general. However, some galaxies still show SF regions in the bar region (NGC 1365 and NGC 1672). We also found that there are Seyfert spaxels that are not just confined to the center, but related to the biconic outflow from the AGN (NGC 1365) or spread inside the bar radius (NGC 1512, NGC 1672) even without the AGN.

### 6.3. Enhanced Emission-line Ratios in the High-velocity Gradient Regions

Our results imply that the emission-line ratios (e.g.,  $[N II]/H\alpha$  and  $[O III]/H\beta$ ) are elevated due to bar-driven shear/shock toward either composite or LINER in the BPT diagram. However, for NGC 1512, the difference between high- and low-velocity gradient regions of the bar is negligible. There can be two reasons for this.

First, the shock velocity and the fraction of shock converted to excite the gas play roles in enhancing the line ratio. Ho et al. (2014) show in their Figure 13 that the line ratios of  $[N II]/H\alpha$ ,  $[S II]/H\alpha$ , and  $[O I]/H\alpha$  increase as the shock velocity increases. Also, within the same shock velocity, the line ratio of  $[O III]/H\beta$  increases as the shock fraction increases, where the shock fraction is the contribution of shock excitation relative to  $H II$  regions. In Section 4, we show that the velocity jump in the high-velocity gradient regions ranges from  $75$ – $170 \text{ km s}^{-1}$ , depending on the objects. Therefore, we would expect high shear regions to show enhanced  $[N II]/H\alpha$  to some degree toward the LINER regime in the BPT diagram. But the shift of  $[N II]/H\alpha$  also depends on the fraction of shock that is converted to change the emission-line ratio, which cannot be readily estimated. Therefore, we infer that the shock fraction might not have been large enough to show a prominent change in the emission-line ratio for NGC 1512.

Second, even though the shear and shock may enhance the line ratio by shock excitation, if the regions already have

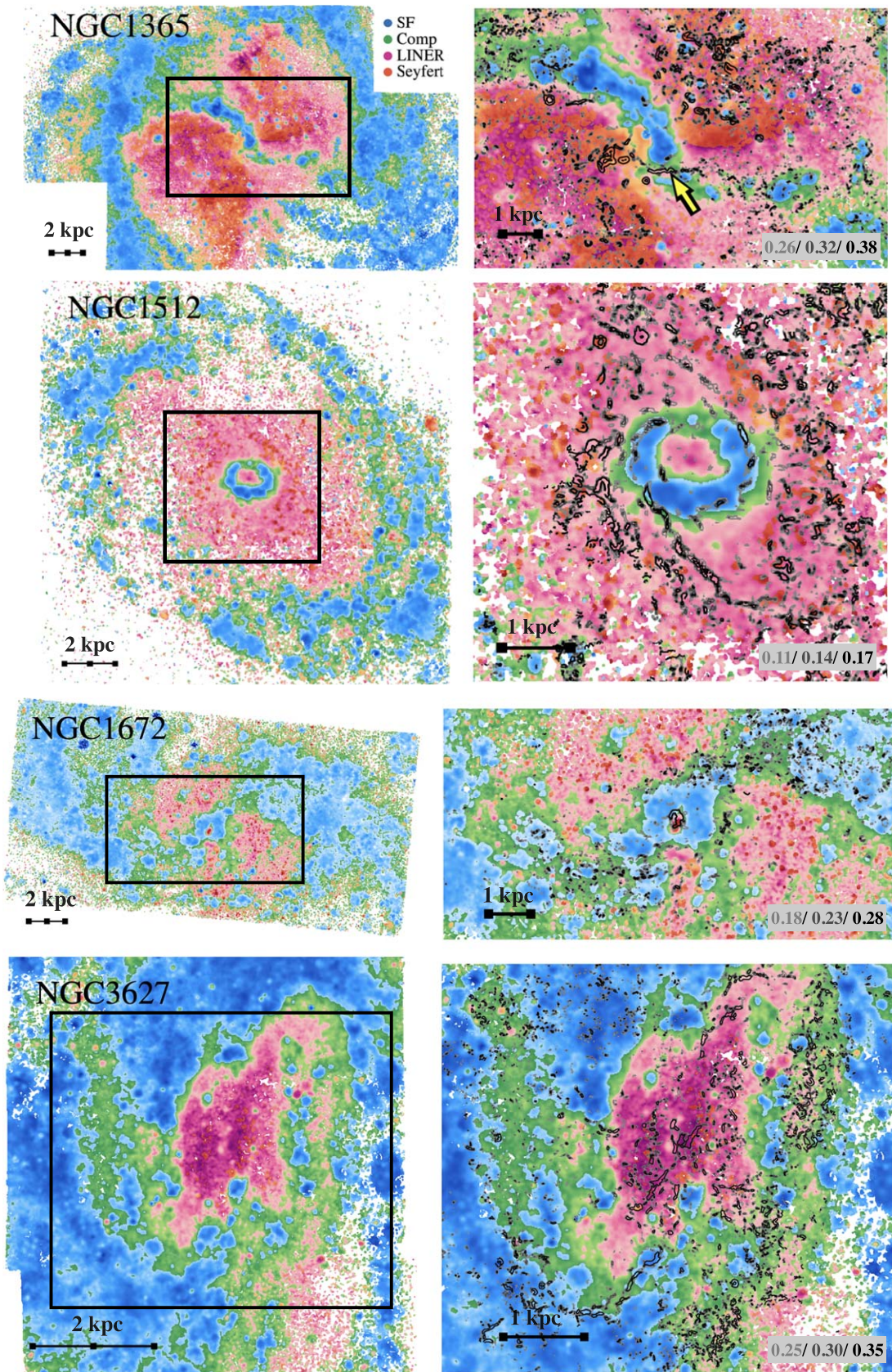


**Figure 10.** BPT maps of the sample galaxies. The right panels are zoomed-in versions of the BPT map overlapped with the velocity gradient contours. Numbers on the bottom right of each panel indicate the contour levels of velocity gradients in  $[\text{km s}^{-1} \text{pc}^{-1}]$ . The color coding is the same as in Figure 9. Blue points indicate SF, red to orange points denote Seyfert, magenta points indicate LINER, and green points represent the composite region.

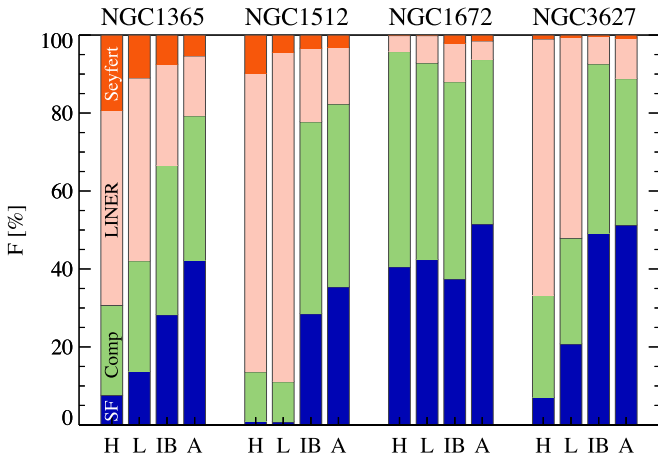


**Figure 11.** Ratio of ionizing sources in different structures of galaxies: high-velocity gradient regions in the bar (H), low-velocity gradient regions in the bar (L), interbar (IB) regions, which are outside the bar but still within the bar radius, and all the other regions of the galaxy (A) for each object. Note that in this bar region of “H” and “L,” bar ends and nuclear regions are excluded to estimate the ratio to focus on regions of bar-driven shear and shock along the bar dust lane.

increased emission-line ratio and located in LINER or Seyfert domain, then it would be difficult to uplift the line ratios. The whole bar of NGC 1512 is dominated by the LINER or Seyfert type emissions judging by the BPT diagnostics.

It should also be noted that enhanced emission-line ratios do not necessarily guarantee that the ionizing source of the regions is shock originated. The leaking of ionizing photons from H II regions is suggested to be able to explain the diffuse ionized gas with LINER-like emissions (Belfiore et al. 2022). Also, ionization by hot evolved stars (e.g., post-AGB) is found to present LINER-like emission (Singh et al. 2013). As post-AGB stars are common in galaxies, their ionizing effect can be observed unless strong radiation from SF or AGN outshines them. As we observe superimposed different ionizing sources along the line of sight, not just on the disk plane but also in the galactic halo, if there is a lack of SF in the disk, we may well be left with the LINER-like emission from the post-AGBs located along the line of sight. The whole bar region of NGC 1512 may consist of old stars. Indeed, Pessa et al. (2023) find that the mean mass-weighted age of the stellar populations in the bar region of NGC 1512 is  $\sim 10$  Gyr.

Recently, Johnston et al. (2023) proposed a novel method to distinguish ionizing sources by using the multidimensional diagnostic diagram, which exploits the classical BPT, velocity dispersion, and equivalent width of  $H\alpha$  (see also Cid Fernandes et al. 2011; D’Agostino et al. 2019). With the multidimensional diagnostics, they categorize a more diverse range of ionization sources, such as the ionization from hot low-mass evolved stars, shocks, elevated kinematics with low emission-line ratio, diffuse ionized gas, in addition to the classical divisions of AGN, LINER, Seyfert, and SF. Applying these multidimensional diagnostics to divide into more detailed classifications is beyond the scope of the current paper as we focus on the impact of bar-driven shear and shock on SF, and we will apply this in the upcoming future paper to explore further the impact of bar dynamics on gas ionization, gas properties such as virial parameter and turbulent pressure.

## 7. Summary and Conclusion

We investigate the impact of bar-driven shocks and shear along the bar dust lane on SF and emission-line ratios by utilizing data from the PHANGS-MUSE and PHANGS-ALMA surveys. Our results can be summarized as follows.

1. We derive velocity gradients using  $H\alpha$  and stellar velocity maps, and find that velocity gradients are enhanced along the bar dust lane where shear and shock are expected to occur. CO intensity peaks coincide with the enhanced velocity gradient regions or slightly offset to the edge of the bar dust lane. Enhanced velocity gradient regions show velocity jumps from 50 to  $150 \text{ km s}^{-1}$ .
2. We examine the velocity gradient versus SFR surface density and find that spaxels with high (low) molecular surface density show high (low) SFR surface density in general. In low-velocity gradient regions, there are various SFR surface density values from low to high. However, as the velocity gradient increases, the range of SFR surface density narrows down such that the maximum SFR surface density decreases with the velocity gradient. Exceptions are nuclear regions and star-forming knots in the inner rings, which protrude out in the trend with enhanced velocity gradients.
3. By comparing the  $H\alpha$  emission-line maps and velocity gradient maps (Figure 7), we find that strong SF does not occur in the high-velocity gradient regions. We apply the BPT diagnostics on a spaxel-by-spaxel basis and find that the fraction of SF spaxels is lower in high-velocity gradient regions in the bar compared to low-velocity gradient regions in the bar and to all the other regions of the galaxy (Figure 11). This implies that SF is inhibited in the high-velocity gradient regions in the bar where shocks and shear are strong.
4. The majority of high-velocity gradient regions are classified into either LINER or composite categories. This may imply that emission-line ratios are elevated due to bar-driven shock or shear. But we cannot rule out that the absence of recent SF results in revealing LINER-like emission line.
5. Our results are consistent with numerical simulations in which bars drive strong shear, and thus, inhibit SF (e.g., Emsellem et al. 2015). Currently, it is not yet clearly known what properties of a barred galaxy control the strength of bar-driven shear and at what shear strength the SF is inhibited. These questions might be answered through further numerical simulations, which will lead us to understand the diverse impact of bars on the SF and galaxy evolution.

## Acknowledgments

We thank the anonymous referee for helpful comments from careful reading that greatly improved this paper. This research was supported by the Basic Science Research Program through the National Research Foundation of Korea (NRF) funded by the Ministry of Education (RS-2023-00240212 and No. 2019R111A3A02062242) and NRF grant funded by the Korean Government Ministry of Science and ICT (MSIT) (No. 2022R1A4A3031306). This work was supported by STFC grants ST/T000244/1 and ST/X001075/1. T.K. acknowledges the

support from the Korea Foundation for Women In Science, Engineering and Technology (WISSET) grant (2022-804) funded by MSIT under the Support for Parental Leave Replacement Jobs. M.Q. and P.S.B. acknowledge support from the Spanish grants PID2019-106027GA-C44 and PID2019-107427GB-C31, respectively, funded by MCIN/AEI/10.13039/501100011033. A.Z. acknowledges financial support by the research projects PID2020-113689GB-I00 and PID2020-114414GB-I00, financed by MCIN/AEI/10.13039/501100011033, the project A-FQM-510-UGR20 financed from FEDER/Junta de Andalucía-Consejería de Transformación Económica, Industria, Conocimiento y Universidades/Proyecto and by the grants P20\_00334 and FQM108, financed by the Junta de Andalucía (Spain). J.N. acknowledges funding from the European Research Council (ERC) under the European Union’s Horizon 2020 research and innovation program (grant agreement No. 694343). J.M.A. acknowledges the support of the Viera y Clavijo Senior program funded by ACIISI and ULL and the support of the Agencia Estatal de Investigación del Ministerio de Ciencia e Innovación (MCIN/AEI/10.13039/501100011033) under grant Nos. PID 2021-128131NB-I00 and CNS2022-135482 and the European Regional Development Fund (ERDF) “A way of making Europe” and the “NextGenerationEU/PRTR.” A.d.L.C. acknowledges financial support from the Spanish Ministry of Science and Innovation (MICINN) to the coBEARD project (PID2021-128131NB-I00). A.d.L.C. also acknowledges financial support from MICINN through the Spanish State Research Agency, under the Severo Ochoa Centers of Excellence Program 2020–2023 (CEX2019-000920-S). L.P.M. thanks FAPESP for grant 2022/

03703-1 and CNPQ for grant 307115/2021-6 for financial support. L.A.S.L. acknowledges CAPES for the support through grant 88887.637633/2021-00 and CNPQ through grant 200469/2022-3. W.T.K. was supported by a grant from the National Research Foundation of Korea (2022R1A2C1004810). M.G.P. acknowledges the support from the Basic Science Research Program through NRF grant Nos. 2019R111A3A02062242 and 2018R1A6A1A06024970) funded by the Ministry of Education, Korea. Based on observations collected at the European Southern Observatory under ESO programs 1100.B-0651, 095.C-0473 and 094.C-0623 (PHANGS-MUSE; PI: Schinnerer), as well as 094.B-0321 (MAGNUM; PI: Marconi) and 097.B-0640 (TIMER; PI: Gadotti). Raw and reduced data are available at the ESO Science Archive Facility.

*Facilities:* VLT:Yepun, ALMA, JWST.

## **Appendix A**

### **Velocity Gradient Perpendicular to the Bar and Parallel to the Bar**

Velocity gradients can be divided into two different components, perpendicular and parallel to the bar. We estimate the parallel velocity gradient ( $\nabla V_x$ ) and perpendicular velocity gradient ( $\nabla V_y$ ) separately and compare them in Figure 12. We reestimate the ratio of the SF group classified by the BPT diagnostics in high- and low-velocity gradient regions and all the other regions of each galaxy with  $\nabla V_x$  and  $\nabla V_y$ , as in Figure 11. We obtain the same results that the ratio of the SF group is lower in high-velocity gradient regions compared to the others.

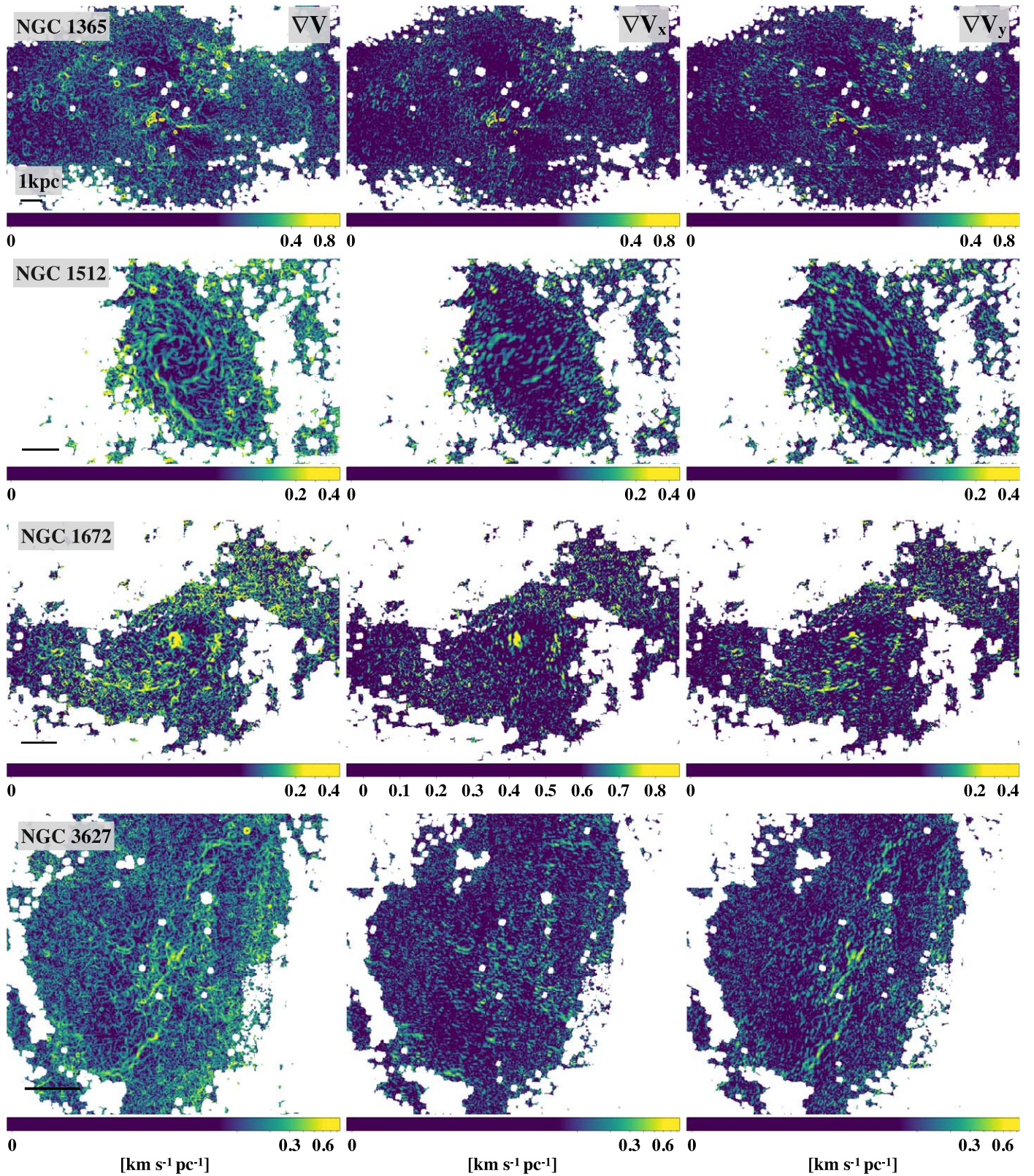


**Figure 12.** The three columns show, respectively, the velocity gradients as in Section 3.1, velocity gradients parallel component to the bar ( $\nabla V_x$ ), and perpendicular to the bar ( $\nabla V_y$ ) in units of  $[\text{km s}^{-1} \text{pc}^{-1}]$ . The black line on the bottom left of each panel spans 1 kpc.



### Appendix B Comparing Velocity Gradients from H $\alpha$ and CO

Velocity gradients can also be obtained using the CO velocity field. However, compared to H $\alpha$ , CO is patchy and only detected marginally along the bar for some galaxies. In order to examine how well H $\alpha$  velocity gradients trace velocity gradients of molecular clouds, we compare velocity gradients from H $\alpha$  ( $\nabla V_{\text{H}\alpha}$ ) and CO ( $\nabla V_{\text{CO}}$ ) in Figure 13.  $\nabla V_{\text{H}\alpha}$  is estimated from the map of ( $V_{\text{H}\alpha} - V_{\text{star}}$ ) and  $\nabla V_{\text{CO}}$  is estimated

with the ( $V_{\text{CO}} - V_{\text{star}}$ ) map following the same steps presented in Section 3.1. CO in the bar of NGC 1512 is marginally detected along the bar; therefore, we could not obtain CO velocity gradients for this object. We find that while there is a spread (especially for low gradients), CO velocity gradients are correlated with H $\alpha$  velocity gradients. This suggests that we can use H $\alpha$  velocity gradients to trace molecular gas velocity gradients for these galaxies.

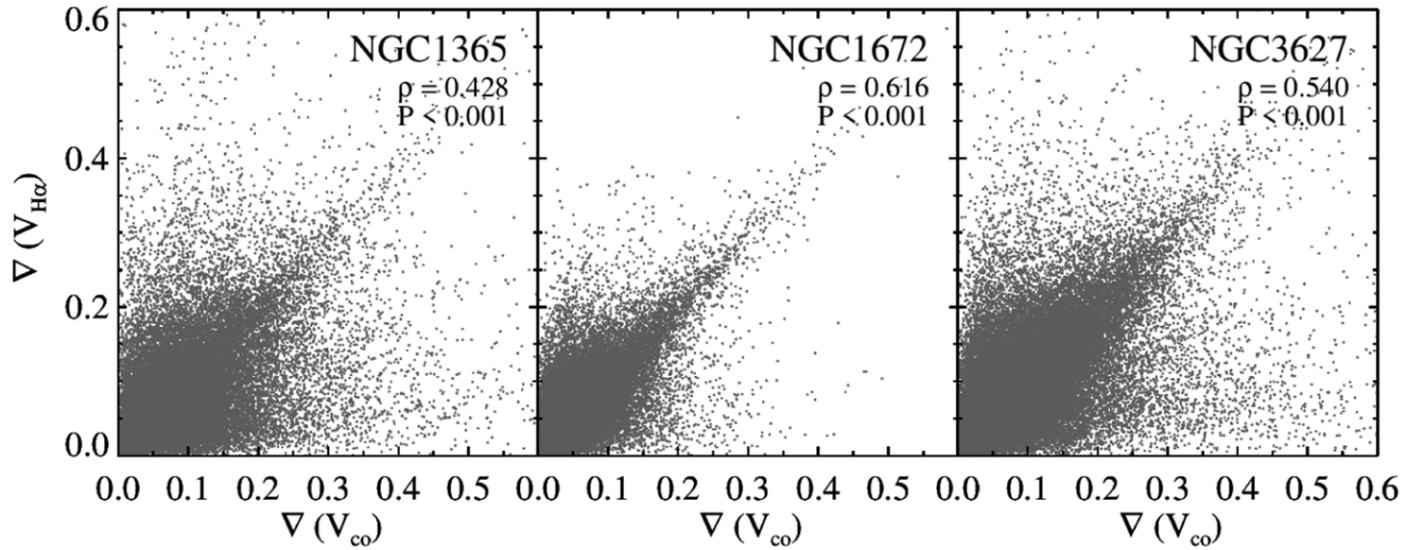
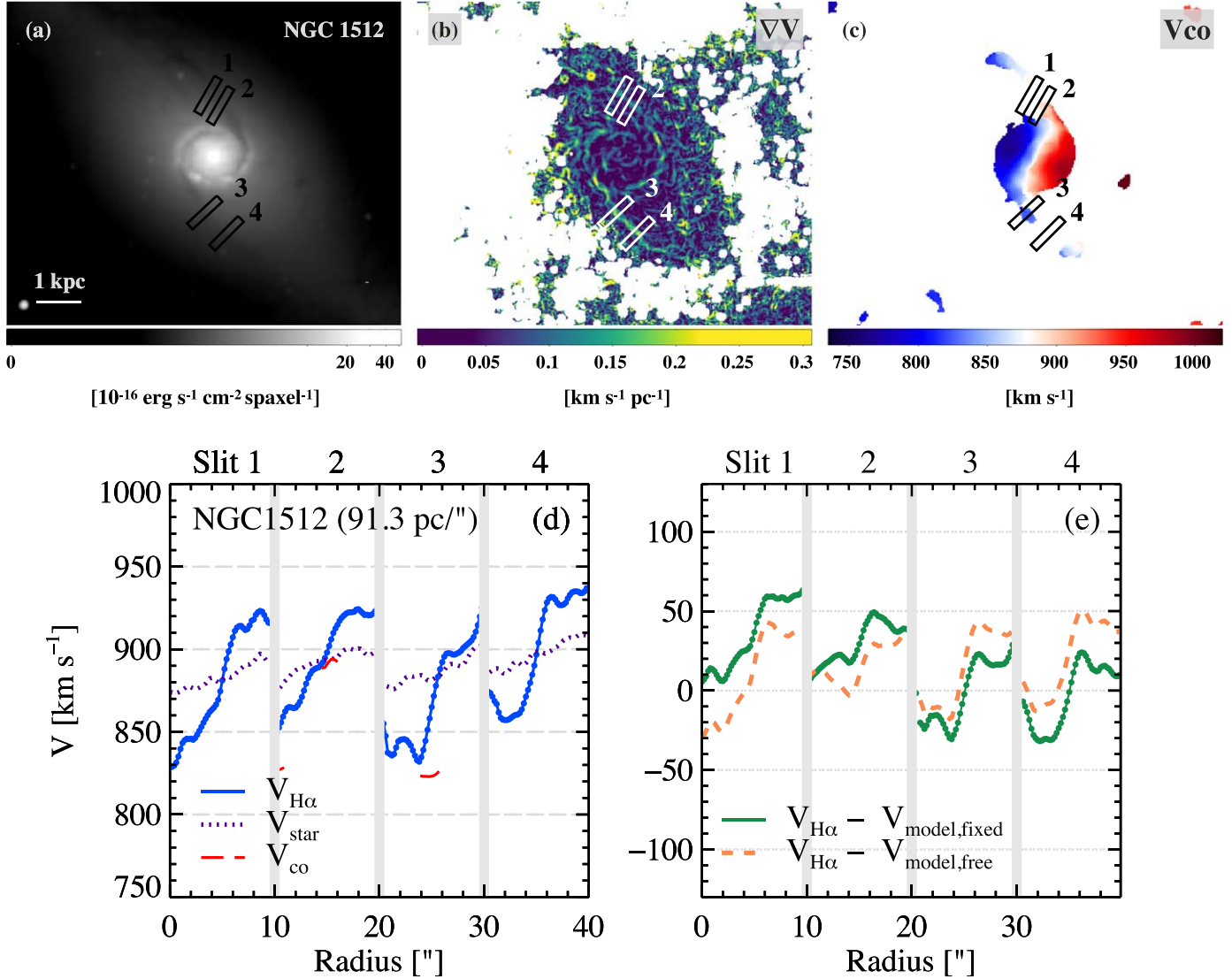


Figure 13. Comparing velocity gradients from  $V_{\text{H}\alpha}$  and  $V_{\text{CO}}$ . Spearman coefficients are presented for each galaxy.

### Appendix C Velocity Jumps for Sample Galaxies

We present velocity jumps on high-velocity gradient regions for the rest of the sample galaxies in Figures 14–16.



**Figure 14.** Velocity jumps in high-velocity gradient regions of NGC 1512. Four pseudo-slits ( $0''.6 \times 10''$ ) are put perpendicular to the high-velocity gradient segments as in the upper panels of the figure. (a): optical image, (b): velocity gradients, (c): CO (2–1) velocity, (d): velocity jumps from south to north (upwards) along the slit of H $\alpha$  (blue solid line), CO (red dashed line, if available), and stellar velocity (purple dotted line), (e): velocity jumps after removal of the galaxy rotation model. Two cases of galaxy rotation models are obtained with 3D-BAROLO, where PAs and inclinations are fixed (green solid line) and set to free (orange dashed line) for each ring. Velocity jumps reach  $50 \text{ km s}^{-1}$  after removal of the galaxy rotation ( $75 \text{ km s}^{-1}$  after deprojection).

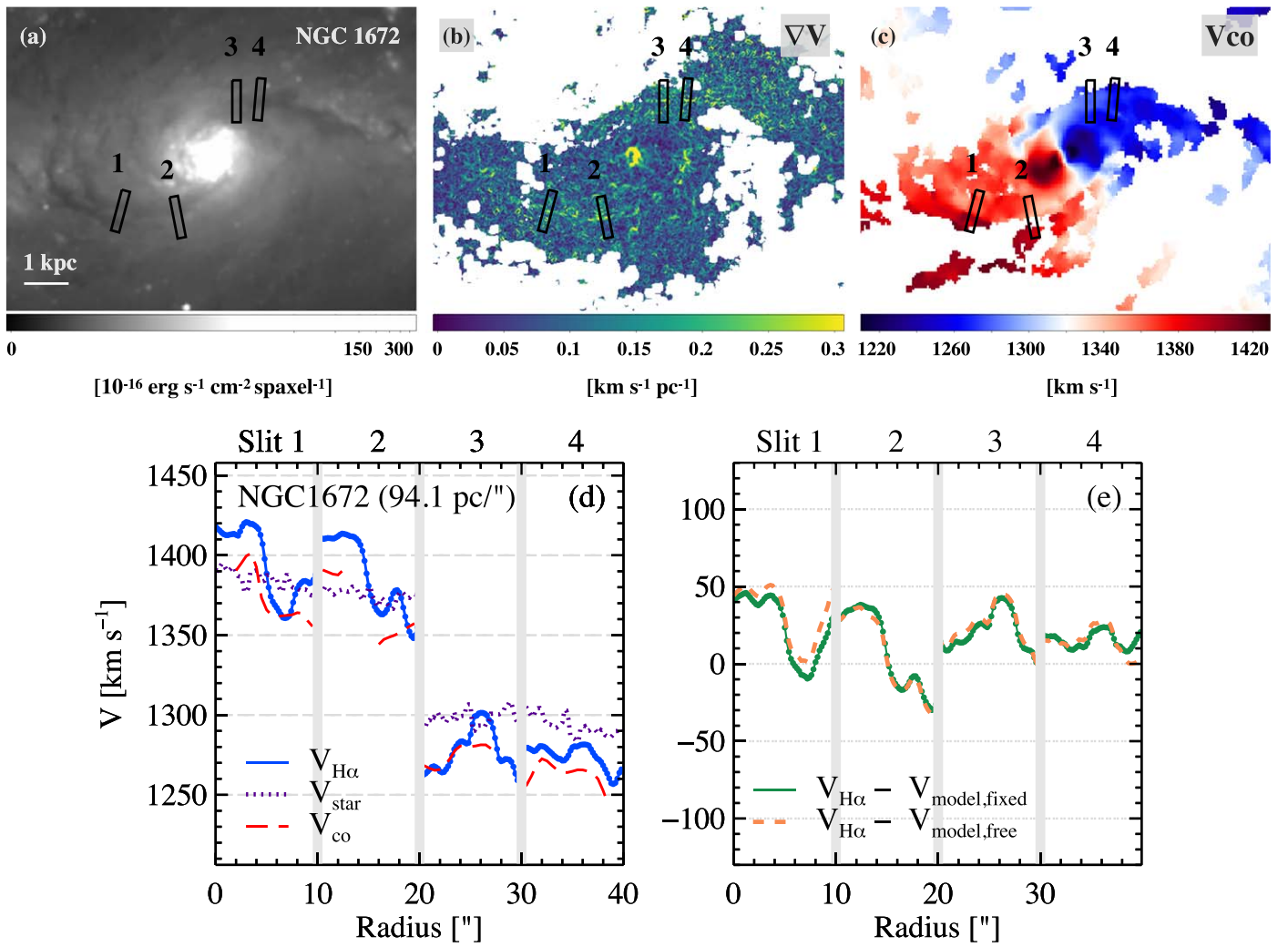
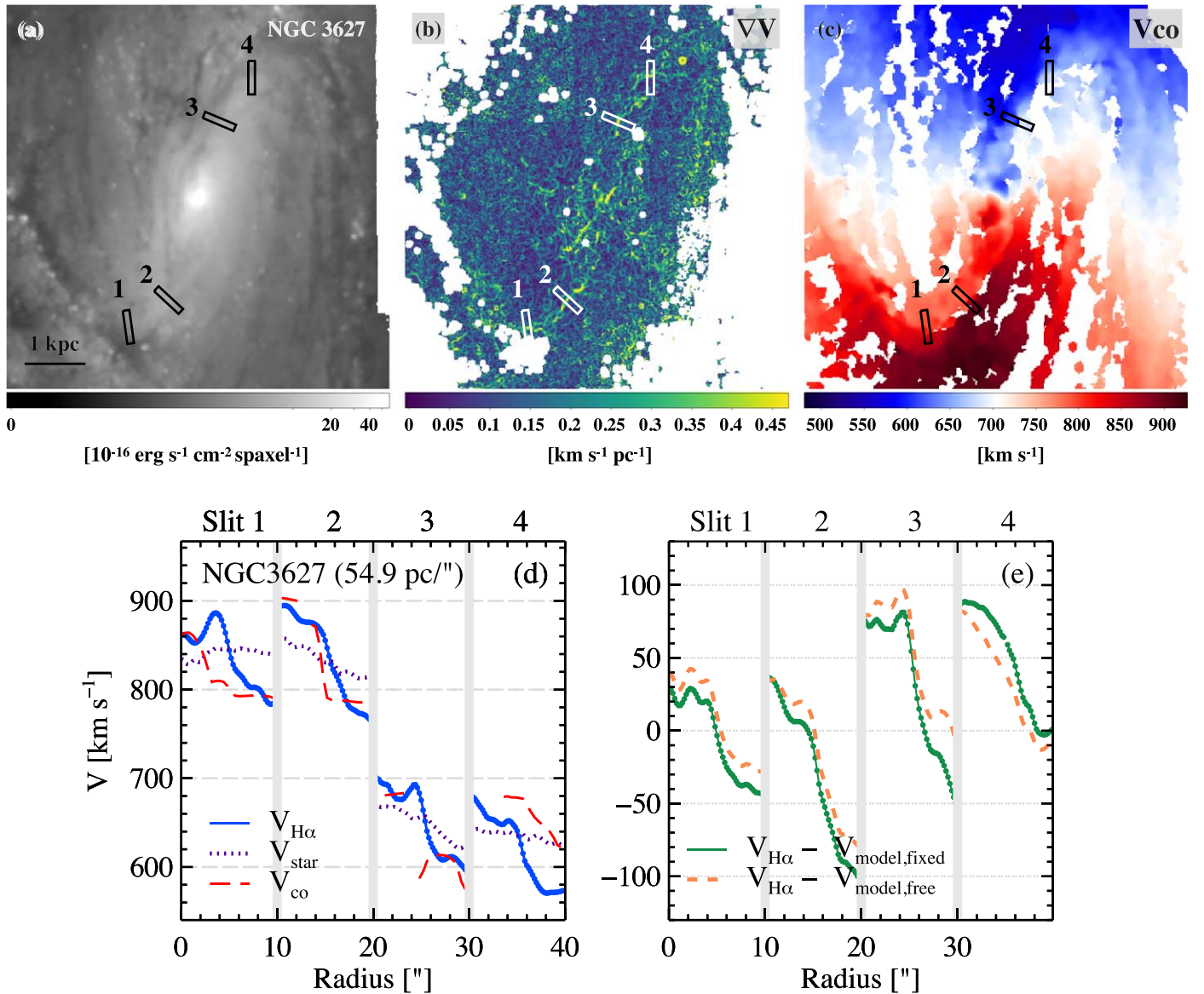


Figure 15. Velocity jumps for NGC 1672 (continued). Velocity jumps reach  $50 \text{ km s}^{-1}$  after removal of the galaxy rotation ( $75 \text{ km s}^{-1}$  after deprojection).



**Figure 16.** Velocity jumps for NGC 3627 (continued). Velocity jumps reach  $80 \text{ km s}^{-1}$  after removal of the galaxy rotation ( $95 \text{ km s}^{-1}$  after deprojection).

## Appendix D Notes on Individual Galaxies

### D.1. NGC 1365

Although there are numerous enhanced velocity gradients that are thought to have originated from the expanding or moving H II regions, velocity gradients along the bar dust lanes are not prominent in the outer part ( $R > 15''$ ) of the galaxy, and are not symmetric. Schinnerer et al. (2023) combined JWST/MIRI, ALMA, and MUSE data and found that the gas inflow onto the central ring is asymmetric and different between the two dust lanes. In addition, they found that in the southern dust lane, young star clusters are rarely found even when abundant molecular gas with properties similar to those of the other dust lane is present. Exactly in this region (marked with a yellow arrow in Figure 10), we found that the velocity gradient is enhanced.

### D.2. NGC 1672

In Figure 8, there are two branches that stick out prominently, one with high  $\Sigma_{\text{mol}}$ , and one with lower  $\Sigma_{\text{mol}}$ .







The branch with high  $\Sigma_{\text{mol}}$ , where the  $\Sigma_{\text{mol}}$  ranges between  $10^{-1}$  and  $10^0$  and the velocity gradients between  $0.2$  and  $0.7 \text{ km s}^{-1}$ , belong to the nuclear region ( $R < 2''5$ ) inside the nuclear ring. In this region, CO (2–1) and H $\alpha$  intensity are high, and also the velocity gradient is extraordinarily high. The elevated velocity gradients may be caused by intense winds from young stars, as appears to be the case in other galaxies with star-bursting nuclear rings, such as NGC 3351 (see Leaman et al. 2019). The other branch with low  $\Sigma_{\text{mol}}$  ( $10^{-3} \sim 10^{-2}$ ) consists of regions around faint H $\alpha$  sources with distinctive velocities.

### D.3. NGC 3627

Enhanced velocity gradients along the dust lane are disconnected at  $R \sim 19''$  ( $\sim 1 \text{ kpc}$ ) on both sides from the center (Figure 4). The elevated velocity gradients in the southern outer part ( $R > 19''$ ) are located at the leading side compared to the CO peaks (Figure 5), but in the inner part ( $R < 19''$ ), they are located at the trailing side compared to the CO intensity. Along the northern part of the bar, enhanced velocity gradients are

located along the trailing side. It is not clear why enhanced velocity gradient regions are located on the trailing side in some parts, especially in this galaxy, as they are located along or at the leading side of the dust lane in other sample galaxies. Gas inflow is found to be reduced when there is a boxy/peanut-shaped bulge (Fragkoudi et al. 2016), and interestingly, the boxy/peanut-shaped bulge of the galaxy spans 18'' (Erwin & Debattista 2016). We suggest that the orbital structures due to the boxy/peanut-shaped bulge and spurs (Erwin & Debattista 2013, 2016) may have an effect on the gas inflow, and may be related to the origin of this offset.

### ORCID iDs

Taehyun Kim  <https://orcid.org/0000-0002-5857-5136>  
 Dimitri A. Gadotti  <https://orcid.org/0000-0003-1775-2367>  
 Miguel Querejeta  <https://orcid.org/0000-0002-0472-1011>  
 Isabel Pérez  <https://orcid.org/0000-0003-1634-4628>  
 Almudena Zurita  <https://orcid.org/0000-0001-6928-6367>  
 Justus Neumann  <https://orcid.org/0000-0002-3289-8914>  
 Glenn van de Ven  <https://orcid.org/0000-0003-4546-7731>  
 Jairo Méndez-Abreu  <https://orcid.org/0000-0002-8766-2597>  
 Adriana de Lorenzo-Cáceres  <https://orcid.org/0000-0002-9744-3486>  
 Patricia Sánchez-Blázquez  <https://orcid.org/0000-0003-0651-0098>  
 Francesca Fragkoudi  <https://orcid.org/0000-0002-0897-3013>  
 Lucimara P. Martins  <https://orcid.org/0000-0002-3666-2810>  
 Luiz A. Silva-Lima  <https://orcid.org/0000-0003-3490-9063>  
 Woong-Tae Kim  <https://orcid.org/0000-0003-4625-229X>  
 Myeong-Gu Park  <https://orcid.org/0000-0003-1544-8556>

### References

- Aguerri, J. A. L., Méndez-Abreu, J., & Corsini, E. M. 2009, *A&A*, 495, 491  
 Anand, G. S., Lee, J. C., Van Dyk, S. D., et al. 2021, *MNRAS*, 501, 3621  
 Athanassoula, E. 1992, *MNRAS*, 259, 345  
 Athanassoula, E., & Misiriotis, A. 2002, *MNRAS*, 330, 35  
 Baker, J. G., & Menzel, D. H. 1938, *ApJ*, 88, 52  
 Baldwin, J. A., Phillips, M. M., & Terlevich, R. 1981, *PASP*, 93, 5  
 Barazza, F. D., Jogee, S., & Marinova, I. 2008, *ApJ*, 675, 1194  
 Beck, R., Ehle, M., Shoutenkov, V., Shukurov, A., & Sokoloff, D. 1999, *Natur*, 397, 324  
 Belfiore, F., Leroy, A. K., Sun, J., et al. 2023, *A&A*, 670, A67  
 Belfiore, F., Santoro, F., Groves, B., et al. 2022, *A&A*, 659, A26  
 Berman, L. 1936, *MNRAS*, 96, 890  
 Beuther, H., Meidt, S., Schinnerer, E., Paladino, R., & Leroy, A. 2017, *A&A*, 597, A85  
 Bigiel, F., Leroy, A. K., Jiménez-Donaire, M. J., et al. 2016, *ApJL*, 822, L26  
 Bittner, A., de Lorenzo-Cáceres, A., Gadotti, D. A., et al. 2021, *A&A*, 646, A42  
 Bolatto, A. D., Warren, S. R., Leroy, A. K., et al. 2013, *Natur*, 499, 450  
 Bosma, A. 1981, *AJ*, 86, 1825  
 Bresolin, F., Rizzi, L., Ho, I. T., et al. 2020, *MNRAS*, 495, 4347  
 Bundy, K., Bershady, M. A., Law, D. R., et al. 2015, *ApJ*, 798, 7  
 Buta, R. J., Sheth, K., Athanassoula, E., et al. 2015, *ApJS*, 217, 32  
 Calzetti, D., Harris, J., Gallagher, J. S. I., et al. 2004, *AJ*, 127, 1405  
 Calzetti, D., Kennicutt, R. C., Engelbracht, C. W., et al. 2007, *ApJ*, 666, 870  
 Cappellari, M., & Emsellem, E. 2004, *PASP*, 116, 138  
 Catalán-Torrecilla, C., Gil de Paz, A., Castillo-Morales, A., et al. 2015, *A&A*, 584, A87  
 Cheung, E., Trump, J. R., Athanassoula, E., et al. 2015, *MNRAS*, 447, 506  
 Cid Fernandes, R., Stasińska, G., Mateus, A., & Vale Asari, N. 2011, *MNRAS*, 413, 1687  
 Cisternas, M., Gadotti, D. A., Knapen, J. H., et al. 2013, *ApJ*, 776, 50  
 Combes, F., & Sanders, R. H. 1981, *A&A*, 96, 164  
 Comerón, S., Salo, H., Laurikainen, E., et al. 2014, *A&A*, 562, A121  
 Contopoulos, G., & Papayannopoulos, T. 1980, *A&A*, 92, 33  
 D'Agostino, J. J., Kewley, L. J., Groves, B. A., et al. 2019, *MNRAS*, 487, 4153  
 de Lorenzo-Cáceres, A., Sánchez-Blázquez, P., Méndez-Abreu, J., et al. 2019, *MNRAS*, 484, 5296  
 de Sá-Freitas, C., Gadotti, D. A., Fragkoudi, F., et al. 2023a, arXiv:2308.04482  
 de Sá-Freitas, C., Gadotti, D. A., Fragkoudi, F., et al. 2023b, *A&A*, 678, A202  
 de Vaucouleurs, G. 1963, *ApJS*, 8, 31  
 den Brok, J. S., Chatzigiannakis, D., Bigiel, F., et al. 2021, *MNRAS*, 504, 3221  
 Di Teodoro, E. M., & Fraternali, F. 2015, *MNRAS*, 451, 3021  
 Díaz-García, S., Lisenfeld, U., Pérez, I., et al. 2021, *A&A*, 654, A135  
 Díaz-García, S., Moyano, F. D., Comerón, S., et al. 2020, *A&A*, 644, A38  
 Díaz-García, S., Salo, H., Laurikainen, E., & Herrera-Endoqui, M. 2016, *A&A*, 587, A160  
 Downes, D., Reynaud, D., Solomon, P. M., & Radford, S. J. E. 1996, *ApJ*, 461, 186  
 Elmegreen, B. G., & Scalo, J. 2004, *ARA&A*, 42, 211  
 Emsellem, E., Renaud, F., Bournaud, F., et al. 2015, *MNRAS*, 446, 2468  
 Emsellem, E., Schinnerer, E., Santoro, F., et al. 2022, *A&A*, 659, A191  
 Englmaier, P., & Gerhard, O. 1997, *MNRAS*, 287, 57  
 Erwin, P., & Debattista, V. P. 2013, *MNRAS*, 431, 3060  
 Erwin, P., & Debattista, V. P. 2016, *ApJL*, 825, L30  
 Eskridge, P. B., Frogel, J. A., Pogge, R. W., et al. 2000, *AJ*, 119, 536  
 Fathi, K., van de Ven, G., Peletier, R. F., et al. 2005, *MNRAS*, 364, 773  
 Feng, Z.-X., Li, Z., Shen, J., et al. 2022, *ApJ*, 933, 233  
 Fragkoudi, F., Athanassoula, E., & Bosma, A. 2016, *MNRAS*, 462, L41  
 Fragkoudi, F., Athanassoula, E., & Bosma, A. 2017, *MNRAS*, 466, 474  
 Fragkoudi, F., Grand, R. J. J., Pakmor, R., et al. 2020, *MNRAS*, 494, 5936  
 Fraser-McKelvie, A., Aragón-Salamanca, A., Merrifield, M., et al. 2020, *MNRAS*, 495, 4158  
 Fujimoto, Y., Tasker, E. J., & Habe, A. 2014, *MNRAS*, 445, L65  
 Gadotti, D. A., Bittner, A., Falcón-Barroso, J., et al. 2020, *A&A*, 643, A14  
 Gadotti, D. A., Sánchez-Blázquez, P., Falcón-Barroso, J., et al. 2019, *MNRAS*, 482, 506  
 Gao, Y., Egusa, F., Liu, G., et al. 2021, *ApJ*, 913, 139  
 Gao, Y., & Solomon, P. M. 2004, *ApJ*, 606, 271  
 Garland, I. L., Fahey, M. J., Simmons, B. D., et al. 2023, *MNRAS*, 522, 211  
 George, K., Joseph, P., Mondal, C., et al. 2020, *A&A*, 644, A79  
 Groves, B., Brinchmann, J., & Walcher, C. J. 2012, *MNRAS*, 419, 1402  
 Hatchfield, H. P., Sormani, M. C., Tress, R. G., et al. 2021, *ApJ*, 922, 79  
 Hawarden, T. G., Mountain, C. M., Leggett, S. K., & Puxley, P. J. 1986, *MNRAS*, 221, 41P  
 Haywood, M., Lehnert, M. D., Di Matteo, P., et al. 2016, *A&A*, 589, A66  
 Hirota, A., Kuno, N., Baba, J., et al. 2014, *PASJ*, 66, 46  
 Ho, I. T., Kewley, L. J., Dopita, M. A., et al. 2014, *MNRAS*, 444, 3894  
 Ho, L. C., Filippenko, A. V., & Sargent, W. L. W. 1997, *ApJ*, 487, 591  
 Hohl, F. 1971, *ApJ*, 168, 343  
 Hong, S., Calzetti, D., Gallagher, J. S. I., et al. 2013, *ApJ*, 777, 63  
 James, P. A., & Percival, S. M. 2018, *MNRAS*, 474, 3101  
 Johnston, V. D., Medling, A. M., Groves, B., et al. 2023, *ApJ*, 954, 77  
 Jorsater, S., Lindblad, P. O., & Boksenberg, A. 1984, *A&A*, 140, 288  
 Kauffmann, G., Heckman, T. M., Tremonti, C., et al. 2003, *MNRAS*, 346, 1055  
 Kennicutt, R. C., & Evans, N. J. 2012, *ARA&A*, 50, 531  
 Kewley, L. J., Dopita, M. A., Sutherland, R. S., Heisler, C. A., & Trevena, J. 2001, *ApJ*, 556, 121  
 Khoperskov, S., Haywood, M., Di Matteo, P., Lehnert, M. D., & Combes, F. 2018, *A&A*, 609, A60  
 Kim, W.-T., Seo, W.-Y., Stone, J. M., Yoon, D., & Teuben, P. J. 2012a, *ApJ*, 747, 60  
 Kim, W.-T., & Stone, J. M. 2012b, *ApJ*, 751, 124  
 Knapen, J. H., Beckman, J. E., Heller, C. H., Shlosman, I., & de Jong, R. S. 1995, *ApJ*, 454, 623  
 Knapen, J. H., Shlosman, I., & Peletier, R. F. 2000, *ApJ*, 529, 93  
 Kolcu, T., Maciejewski, W., Gadotti, D. A., et al. 2023, *MNRAS*, 524, 207  
 Kraljic, K., Bournaud, F., & Martig, M. 2012, *ApJ*, 757, 60  
 Krishnarao, D., Tremonti, C., Fraser-McKelvie, A., et al. 2020, *ApJ*, 898, 116  
 Krumholz, M. R., & Federrath, C. 2019, *FrASS*, 6, 7  
 Laine, S., Kenney, J. D. P., Yun, M. S., & Gottesman, S. T. 1999, *ApJ*, 511, 709  
 Laine, S., Shlosman, I., Knapen, J. H., & Peletier, R. F. 2002, *ApJ*, 567, 97  
 Lang, P., Meidt, S. E., Rosolowsky, E., et al. 2020, *ApJ*, 897, 122  
 Leaman, R., Fragkoudi, F., Querejeta, M., et al. 2019, *MNRAS*, 488, 3904  
 Lee, J. C., Sandstrom, K. M., Leroy, A. K., et al. 2023, *ApJL*, 944, L17  
 Lee, Y. H., Ann, H. B., & Park, M.-G. 2019, *ApJ*, 872, 97  
 Leroy, A. K., Hughes, A., Liu, D., et al. 2021a, *ApJS*, 255, 19  
 Leroy, A. K., Schinnerer, E., Hughes, A., et al. 2021b, *ApJS*, 257, 43  
 Leroy, A. K., Walter, F., Sandstrom, K., et al. 2013, *AJ*, 146, 19  
 López-Cobá, C., Sánchez, S. F., Lin, L., et al. 2022, *ApJ*, 939, 40  
 Maeda, F., Egusa, F., Ohta, K., Fujimoto, Y., & Habe, A. 2023, *ApJ*, 943, 7

- Maeda, F., Ohta, K., Fujimoto, Y., Habe, A., & Ushio, K. 2020, *MNRAS*, **495**, 3840
- Maeda, F., Ohta, K., Fujimoto, Y., & Habe, A. 2021, *MNRAS*, **502**, 2238
- Martin, P., & Friedli, D. 1997, *A&A*, **326**, 449
- Masters, K. L., Nichol, R. C., Hoyle, B., et al. 2011, *MNRAS*, **411**, 2026
- McKee, C. F., & Ostriker, E. C. 2007, *ARA&A*, **45**, 565
- Menéndez-Delmestre, K., Sheth, K., Schinnerer, E., Jarrett, T. H., & Scoville, N. Z. 2007, *ApJ*, **657**, 790
- Momose, R., Okumura, S. K., Koda, J., & Sawada, T. 2010, *ApJ*, **721**, 383
- Mundell, C. G., & Shone, D. L. 1999, *MNRAS*, **304**, 475
- Muraoka, K., Kohno, K., Tosaki, T., et al. 2009, *PASJ*, **61**, 163
- Muraoka, K., Sorai, K., Kuno, N., et al. 2016, *PASJ*, **68**, 89
- Muraoka, K., Sorai, K., Miyamoto, Y., et al. 2019, *PASJ*, **71**, S15
- Neumann, J., Gadotti, D. A., Wisotzki, L., et al. 2019, *A&A*, **627**, A26
- Ostriker, J. P., & Peebles, P. J. E. 1973, *ApJ*, **186**, 467
- Pence, W. D., & Blackman, C. P. 1984, *MNRAS*, **207**, 9
- Pessa, I., Schinnerer, E., Leroy, A. K., et al. 2022, *A&A*, **663**, A61
- Pessa, I., Schinnerer, E., Sanchez-Blazquez, P., et al. 2023, *A&A*, **673**, A147
- Peterson, C. J., & Huntley, J. M. 1980, *ApJ*, **242**, 913
- Phillips, M. M., Turtle, A. J., Edmunds, M. G., & Pagel, B. E. J. 1983, *MNRAS*, **203**, 759
- Querejeta, M., Schinnerer, E., Meidt, S., et al. 2021, *A&A*, **656**, A133
- Regan, M. W., Sheth, K., & Vogel, S. N. 1999, *ApJ*, **526**, 97
- Regan, M. W., Vogel, S. N., & Teuben, P. J. 1997, *ApJL*, **482**, L143
- Relaño, M., & Beckman, J. E. 2005, *A&A*, **430**, 911
- Renaud, F., Bournaud, F., Emsellem, E., et al. 2015, *MNRAS*, **454**, 3299
- Reynaud, D., & Downes, D. 1998, *A&A*, **337**, 671
- Roberts, W. W. J., Huntley, J. M., & van Albada, G. D. 1979, *ApJ*, **233**, 67
- Rozas, M., Zurita, A., Beckman, J. E., & Pérez, D. 2000, *A&AS*, **142**, 259
- Salo, H., Laurikainen, E., Buta, R., & Knapen, J. H. 2010, *ApJL*, **715**, L56
- Salo, H., Laurikainen, E., Laine, J., et al. 2015, *ApJS*, **219**, 4
- Sánchez, S. F., Kennicutt, R. C., Gil de Paz, A., et al. 2012, *A&A*, **538**, A8
- Schinnerer, E., Emsellem, E., Henshaw, J. D., et al. 2023, *ApJL*, **944**, L15
- Scoville, N. Z., Sanders, D. B., & Clemens, D. P. 1986, *ApJL*, **310**, L77
- Seo, W.-Y., Kim, W.-T., Kwak, S., et al. 2019, *ApJ*, **872**, 5
- Sheth, K., Melbourne, J., Elmegreen, D. M., et al. 2012, *ApJ*, **758**, 136
- Sheth, K., Regan, M. W., Vogel, S. N., & Teuben, P. J. 2000, *ApJ*, **532**, 221
- Sheth, K., Vogel, S. N., Regan, M. W., Thornley, M. D., & Teuben, P. J. 2005, *ApJ*, **632**, 217
- Shull, J. M., & McKee, C. F. 1979, *ApJ*, **227**, 131
- Silva-Lima, L. A., Martins, L. P., Coelho, P. R. T., & Gadotti, D. A. 2022, *A&A*, **661**, A105
- Singh, R., van de Ven, G., Jahnke, K., et al. 2013, *A&A*, **558**, A43
- Solomon, P. M., Downes, D., & Radford, S. J. E. 1992, *ApJL*, **398**, L29
- Sorai, K., Kuno, N., Nishiyama, K., et al. 2012, *PASJ*, **64**, 51
- Sormani, M. C., Barnes, A. T., Sun, J., et al. 2023, *MNRAS*, **523**, 2918
- Sormani, M. C., Binney, J., & Magorrian, J. 2015, *MNRAS*, **449**, 2421
- Sormani, M. C., Sobacchi, E., Fragkoudi, F., et al. 2018a, *MNRAS*, **481**, 2
- Sormani, M. C., Treß, R. G., Glover, S. C. O., et al. 2019, *MNRAS*, **488**, 4663
- Sormani, M. C., Treß, R. G., Ridley, M., et al. 2018b, *MNRAS*, **475**, 2383
- Spinoso, D., Bonoli, S., Dotti, M., et al. 2017, *MNRAS*, **465**, 3729
- Stone, M. E. 1970, *ApJ*, **159**, 277
- Storchi-Bergmann, T., & Schnorr-Müller, A. 2019, *NatAs*, **3**, 48
- Sun, J., Leroy, A. K., Schinnerer, E., et al. 2020, *ApJL*, **901**, L8
- Tubbs, A. D. 1982, *ApJ*, **255**, 458
- Usero, A., Leroy, A. K., Walter, F., et al. 2015, *AJ*, **150**, 115
- Veilleux, S., & Osterbrock, D. E. 1987, *ApJS*, **63**, 295
- Venturi, G., Nardini, E., Marconi, A., et al. 2018, *A&A*, **619**, A74
- Verley, S., Combes, F., Verdes-Montenegro, L., Bergond, G., & Leon, S. 2007, *A&A*, **474**, 43
- Watkins, E. J., Barnes, A. T., Henny, K., et al. 2023, *ApJL*, **944**, L24
- Weiner, B. J., Williams, T. B., van Gorkom, J. H., & Sellwood, J. A. 2001, *ApJ*, **546**, 916
- Yajima, Y., Sorai, K., Kuno, N., et al. 2019, *PASJ*, **71**, S13
- Zánmar Sánchez, R., Sellwood, J. A., Weiner, B. J., & Williams, T. B. 2008, *ApJ*, **674**, 797
- Zee, W.-B. G., Paudel, S., Moon, J.-S., & Yoon, S.-J. 2023, *ApJ*, **949**, 91
- Zurita, A., Relaño, M., Beckman, J. E., & Knapen, J. H. 2004, *A&A*, **413**, 73